





High-Resolution Finite Fault Slip Inversion of the 2019 Ridgecrest Earthquake Using 3D Finite Element Modeling

Magali Barba-Sevilla^{1,2} , Margaret T. Glasscoe³, Jay Parker⁴ , Gregory A. Lyzenga⁴, Michael J. Willis^{1,2} , and Kristy F. Tiampo^{1,2} 

¹Cooperative Institute for Research in Environmental Sciences, University of Colorado Boulder, Boulder, CO, USA,

²Department of Geological Sciences, University of Colorado Boulder, Boulder, CO, USA, ³Earth Systems Science Center, University of Alabama in Huntsville, Huntsville, AL, USA, ⁴Jet Propulsion Laboratory, California Institute of Technology, Pasadena, CA, USA

Key Points:

- High resolution finite element model with complex rheology and fused synthetic aperture radar-Global Navigation Satellite System data produces a more complete fault slip model at all depths
- Magnitude and extent of maximum slip regions surrounding the hypocenter persist for both homogeneous and heterogeneous rheology types
- Maximum slip is bounded by mainshock hypocenter, aftershocks, decreased Poisson's ratio bodies, and the seismogenic zone

Supporting Information:

Supporting Information may be found in the online version of this article.

Correspondence to:

M. Barba-Sevilla,
magali.barba@colorado.edu

Citation:

Barba-Sevilla, M., Glasscoe, M. T., Parker, J., Lyzenga, G. A., Willis, M. J., & Tiampo, K. F. (2022). High-resolution finite fault slip inversion of the 2019 Ridgecrest earthquake using 3D finite element modeling. *Journal of Geophysical Research: Solid Earth*, 127, e2022JB024404. <https://doi.org/10.1029/2022JB024404>

Received 19 MAR 2022

Accepted 2 SEP 2022

Author Contributions:

Conceptualization: Magali Barba-Sevilla, Margaret T. Glasscoe, Jay Parker, Kristy F. Tiampo

Data curation: Magali Barba-Sevilla

Formal analysis: Magali Barba-Sevilla, Jay Parker, Michael J. Willis, Kristy F. Tiampo

Funding acquisition: Magali Barba-Sevilla, Margaret T. Glasscoe, Kristy F. Tiampo

Investigation: Magali Barba-Sevilla, Margaret T. Glasscoe, Jay Parker, Gregory A. Lyzenga, Michael J. Willis, Kristy F. Tiampo

Abstract The 2019 Ridgecrest earthquake sequence manifested as one of the most complex fault surface ruptures observed in California in modern times. The M6.4 foreshock and M7.1 mainshock occurred on an intricate network of orthogonal and sub-parallel faults resulting in observable surface displacement and surface rupture captured by geodetic data. Here we present the application of a high-resolution 3D finite element model (FEM) approach to invert for the detailed fault slip of the entire sequence using complex rheology and fused coseismic Global Navigation Satellite System (GNSS) data with Sentinel-1 differential interferometric synthetic aperture radar and pixel offset data. The heterogeneous FEM and the fused geodetic data set of pixel offsets, interferograms, and GNSS data results in our optimal inversion solution. This preferred solution is a complex, high-resolution non-planar slip model of both the M6.4 and M7.1 events that features three main regions of large slip (6.9+ m), with depths ranging from 2 to 10 km. The regions of slip are bounded by the mainshock hypocenter and the mainshock aftershocks and appear to be related to spatially varying rheological properties. We successfully reproduce a localized region of observed subsidence in the northern portion of the primary fault through the inclusion of a curved fault strand with a significant dip-slip component. The curved fault strand is the site of our maximum slip of 7.4 m at a depth of 4.2 km. The results demonstrate a robust fit from a more complete, detailed model for the entire seismogenic zone with reasonable computational cost, providing new insights into the governing rheologic and structural processes.

Plain Language Summary The 2019 Ridgecrest, California earthquake sequence consisted of two main earthquakes: the M6.4 foreshock and the M7.1 mainshock. Understanding the structure and behavior of the faults responsible for these earthquakes is important to earthquake hazard and forecasting. We construct a complex 3D model representing the earth's interior at the location of the Ridgecrest earthquake using triangular building blocks. By combining Global Positioning System and different microwave remote sensing data, we produce a detailed map of how the ground deformed, even close to the faults. We use this deformation map to fine tune our 3D model and determine in which direction and by how much the faults moved during the M6.4 and M7.1 earthquakes. We find that the faults had large movement of almost 7 m in three regions at depths of 2–10 km. The largest movement of 7.4 m occurs north of the mainshock at an offshoot of the main fault where our mapped deformation shows the ground sinking. The locations of large fault movement coincide with regions of low aftershock activity and particular earth material.

1. Introduction

The 4–6 July, 2019 M_w 7.1 Ridgecrest earthquake sequence of Searles Valley is the third major sequence to take place within the Eastern California Shear Zone (ECSZ) in recent history. The Ridgecrest earthquake occurred 20 years after the 1999 M_w 7.1 Hector Mine earthquake and 27 years after the 1992 Landers earthquake sequence, which included the M_w 6.1 Joshua Tree foreshock (23 April 1992), the M_w 7.3 Landers mainshock (28 June 1992), and the M_w 6.2 Big Bear aftershock (28 June 1992) (Hauksson et al., 1993). Like its predecessors, the Ridgecrest earthquake was a predominately right-lateral strike-slip event on a network of NW-SE oriented faults, consistent with the dominant deformation in the ECSZ. In addition to the July 6 (03:19:53 UTC) M_w 7.1 mainshock, the Ridgecrest earthquake sequence also featured a M_w 6.4 left-lateral foreshock on July 4 (17:33:49 UTC). This strong foreshock ruptured a series of NE-SW oriented faults, orthogonal to the mainshock rupture at its

Methodology: Magali Barba-Sevilla, Margaret T. Glasscoe, Jay Parker, Gregory A. Lyzenga, Kristy F. Tiampo

Project Administration: Margaret T. Glasscoe, Jay Parker, Kristy F. Tiampo

Resources: Magali Barba-Sevilla, Margaret T. Glasscoe, Kristy F. Tiampo

Software: Magali Barba-Sevilla, Margaret T. Glasscoe, Jay Parker, Gregory A. Lyzenga

Supervision: Margaret T. Glasscoe, Jay Parker, Kristy F. Tiampo

Validation: Magali Barba-Sevilla, Jay Parker, Gregory A. Lyzenga, Kristy F. Tiampo

Visualization: Magali Barba-Sevilla
Writing – original draft: Magali Barba-Sevilla

Writing – review & editing: Magali Barba-Sevilla, Margaret T. Glasscoe, Jay Parker, Gregory A. Lyzenga, Michael J. Willis, Kristy F. Tiampo

southernmost end (Figure 1). This cross-faulting was also observed in the Landers sequence; however, unlike the Ridgecrest sequence, the Landers right-lateral mainshock preceded the left-lateral Big Bear aftershock.

The active deformation and high seismicity within the ECSZ is driven by the stress and strain resulting from the annual ~ 50 mm relative motion between the Pacific and North American plates (DeMets & Dixon, 1999). Accommodating nearly 25% of the relative plate motion, the ECSZ is second only to the San Andreas Fault (SAF), which is the surface manifestation of the dominant plate boundary (Dokka & Travis, 1990; Sauber et al., 1986, 1994). The ECSZ extends as far north as Owens Valley and as far south as the Mojave Desert. It is bounded by the SAF and Sierra Nevada on the west and the Basin and Range on the east. The NE-SW trending Garlock fault separates the ECSZ into the Walker Lane (WL) region to the north and the Mojave block region to the south. The Ridgecrest earthquake sequence occurred within the southernmost section of the Walker Lane portion of the ECSZ (Liu et al., 2010; Dixon & Xie, 2018), rupturing a complex series of unmapped conjugate faults (Stewart et al., 2019).

Fortunately, these largely unforeseen earthquakes occurred in a sparsely populated area, resulting in relatively little damage and no deaths. Nonetheless, these events reveal how little we know about this geologically young fault zone and its role in the SAF system. Accurately characterizing the Ridgecrest earthquake sequence in all its complexity is essential to earthquake forecasting and regional seismic hazard modeling.

The Ridgecrest earthquake sequence is the best recorded event in the United States to date, generating extensive, high-quality datasets (Taira & Bent, 2020). Data collected include time-sensitive fault mapping and field observations (Duross et al., 2020; Ponti et al., 2020; Stewart et al., 2019); structure from motion surveys (Donnellan et al., 2020); static offset and high-rate Global Navigation Satellite System (GNSS) (Brooks et al., 2020; Mattioli et al., 2020; Melgar et al., 2019); synthetic aperture radar (SAR), Sentinel-1 A/B, COSMOS-SkyMed, ALOS-2 (Chen et al., 2020; Jin & Fialko, 2020; Tung et al., 2021; Wang et al., 2020); optical, Planet Labs (Barnhart et al., 2019; Milliner & Donnellan, 2020), WorldView (Antoine et al., 2021; Barnhart et al., 2019), Pleiades (Antoine et al., 2021), and Sentinel-2 (Barnhart et al., 2019); LIDAR (Hudnut et al., 2020); borehole strainmeter recordings (Pollitz et al., 2020); and strong motion waveform data (Liu et al., 2019). This assortment of data has led to a considerable number of studies evaluating the coseismic fault slip of the event using diverse modeling approaches and data combinations. Despite differing data and methodology, the majority of literature (Barnhart et al., 2019; Goldberg et al., 2020; Liu et al., 2019; Magen et al., 2020; Pollitz et al., 2020) feature fault slip models characterized by a peak slip of 4–6 m within 15 km of the hypocenter at depths in the uppermost 10 km. A few studies propose a larger peak slip of 7–9 m in the same general location (Qiu et al., 2020; Ross et al., 2019; Tung et al., 2021).

Several of these studies used multiple rectangular fault segments of constant strike to approximate the curved fault geometry (Feng et al., 2020; Jin & Fialko, 2020; Liu et al., 2010; Magen et al., 2020; Pollitz et al., 2020; Qiu et al., 2020; Ross et al., 2019). Alternatively, Barnhart et al. (2019) and Goldberg et al. (2020) use triangular elements to discretize the mainshock and foreshock fault planes; however, the preferred mainshock model in Barnhart et al. (2019) uses a single continuous fault with varying strike and dip, while Goldberg et al. (2020) uses four faults with a vertical dip. Although Tung et al. (2021) constructs complex continuous curvilinear fault surfaces using a Finite Element Model (FEM) mesh incorporating complex rheology, the fault model is limited to the primary mainshock (NWF) and foreshock (SWF) fault strands. Furthermore, Tung et al. (2021) limits their analysis to Interferometric Synthetic Aperture Radar (InSAR) data, without incorporating the near-field pixel offsets where InSAR coherence is less than 0.4.

While both triangular element derived Green's functions and FEM derived Green's functions can be used to honor complex fault geometries, FEM derived Green's functions have the unique ability to incorporate detailed rheology. FEM derived Green's functions have been applied to deriving slip for various stages of the earthquake cycle, including the coseismic (Currenti et al., 2008; Hashima et al., 2016; Hsu et al., 2011; Masterlark, 2003; Masterlark & Hughes, 2008; Tung & Masterlark, 2018; Tung et al., 2021), interseismic (Williams & McCaffrey, 2001; Williams & Wallace, 2015, 2018; Zhu & Zhang, 2013), and postseismic (Freed, 2007; Masterlark et al., 2001; Takeuchi & Fialko, 2013) periods.

Our study is the first to use a high-resolution 3D FEM with multisegment fault geometry, detailed rheology, and fused geodetic data observations composed of pixel offsets, InSAR, and GNSS data to solve for finite fault slip for the Ridgecrest sequence. We reproduce the complex geometry of the Ridgecrest earthquake fault rupture by using satellite imagery fault-rupture data to constrain the multisegment fault geometry in great

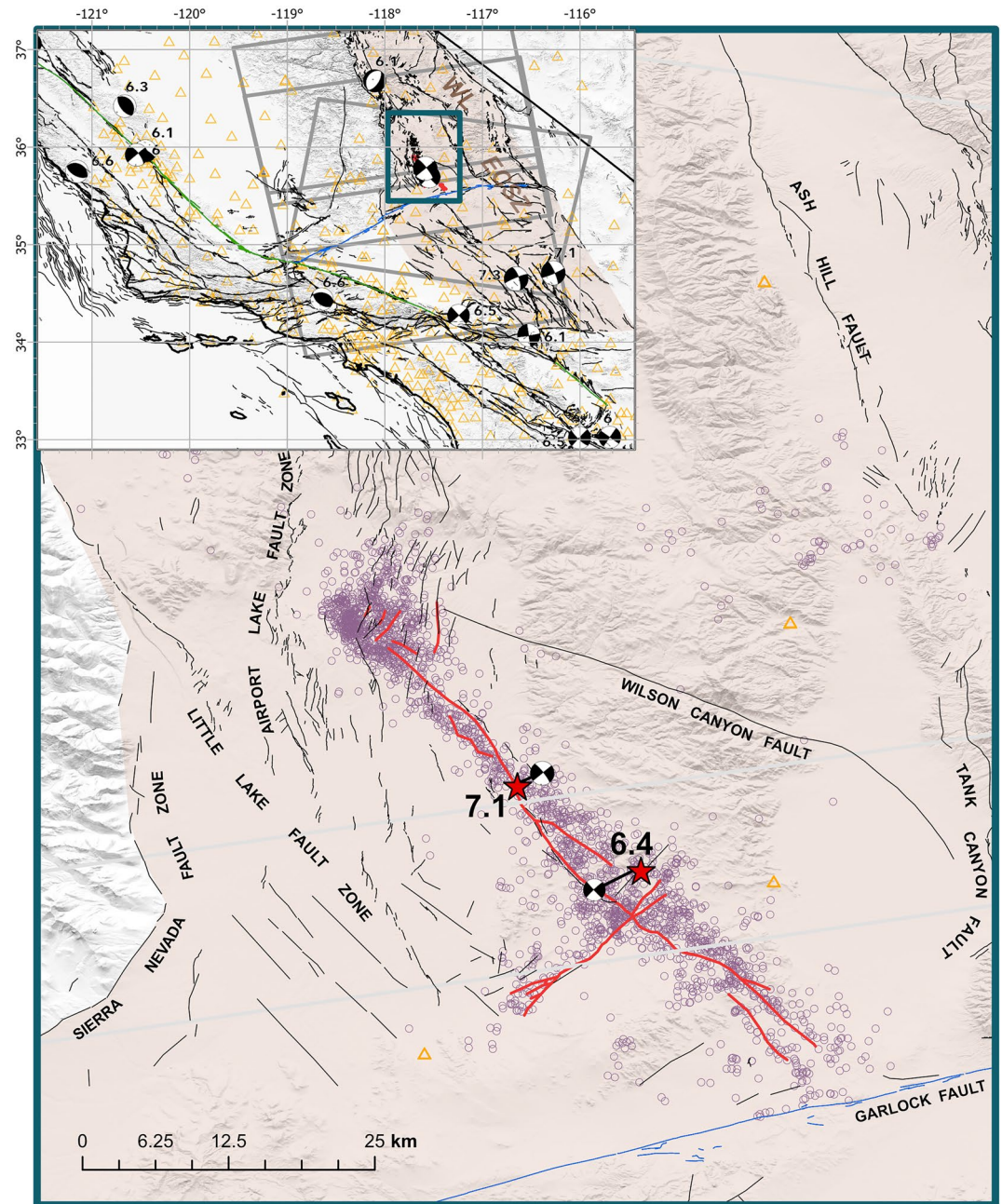


Figure 1. Overview maps of the Ridgecrest earthquake sequence and tectonic setting. Teal rectangle in inset map outlines the location of larger map with sequence details. Maps feature surface fault rupture trace (red line) (SCEC Ridgecrest Event Response, Mike Oskin), Global CMT focal mechanisms for $M_w \geq 6$ earthquakes since 1976 plotted at centroid locations, regional (<40 km from mainshock) $M2.5+$ aftershocks spanning one year after $M6.4$ event (purple circles). Epicenters (red stars) for $M7.1$ and $M6.4$ are shown and linked to their CMT focal mechanism. Also plotted are the synthetic aperture radar data footprints (gray rectangles) and Global Navigation Satellite System stations (orange triangles), the Eastern California Shear Zone-Walker Lane (transparent tan region), and Quaternary faults (black lines), including San Andreas (green line) and Garlock faults (blue line), from the Fault Activity Map of California. Background imagery is DEM hillshade from USGS The National Map: 3D Elevation Program.

detail through high-resolution discretization of 500 m at the fault surface. Our detailed multisegment model uniquely captures the right-step in the northern portion of the main fault rupture responsible for the significant 1.1 m of coseismic subsidence in a predominately right-lateral event. Additionally, our study solves for variable rake and inverts for optimal fault dip while other studies (Goldberg et al., 2020; Liu et al., 2019; Pollitz

Table 1
Synthetic Aperture Radar Data Overview

Sensor	Direction	Path	Frame	Date (yyyy/ mm/dd)	Start time (UTC)	Stop time (UTC)
S1A	ASC	64	109	2019/07/04	01:50:23	01:50:51
S1A	ASC	64	114	2019/07/04	01:50:49	01:51:16
S1A	DSC	71	474	2019/07/04	13:51:58	13:52:25
S1B	ASC	64	113	2019/07/10	01:49:59	01:50:26
S1A	DSC	71	474	2019/07/16	13:51:59	13:52:26

et al., 2020; Qiu et al., 2020) simplify their mainshock inversions to pure strike-slip motion on vertically dipping faults. Lastly, our study provides a detailed analysis on the effects of complex rheology on the final slip solutions.

In this paper, we present our 3D FEM inversion approach to characterizing the Ridgecrest earthquake sequence. In Section 2, we provide an overview of the geodetic data used in the inversion. Section 3 describes the FEM inversion methodology, including the construction of the fault mesh and domain, the calculation of Green's functions from the FEM, our least squares inversion approach to solving for slip and variable rake, and the geodetic data integration into a single fused 3D displacement data set. Section 4 presents the inverted slip and rake and outlines the performance of the inversion while Section 5 evaluates the results relative to other studies and ground-based field observations.

2. Geodetic Displacement Data

For our study, we exploit both Nevada Geodetic Laboratory (NGL) Global Positioning System (GPS) Coseismic Displacement 5 min Solutions and coseismic ESA Sentinel-1 A/B SAR imagery. The arid to semi-arid desert and sparsely vegetated setting of the earthquake make it the ideal location for achieving high coherence using C-band SAR imagery (Barnhart et al., 2019; Jin & Fialko, 2020; Wang et al., 2020). We use five single-look complex (SLC) SAR images, two ascending and one descending preseismic SLCs and one ascending and one descending postseismic SLC (Table 1). The two ascending preseismic SLCs are stitched to cover our entire region of interest. From these SLCs, we generate eight products: ascending and descending interferograms and coherence images (Figure 2), ascending range and azimuth offsets, and descending range and azimuth offsets (Figure 3). The geocoded unwrapped, topo-corrected interferograms and pixel offsets were produced using the topsApp workflow in the Jet Propulsion Laboratory (JPL) InSAR Scientific Computing Environment (ISCE) (Rosen et al., 2012). Processing steps accomplished within the standard ISCE topsApp workflow include cropping SLCs, frame and subswath stitching, multilooking data to 13 looks in range and two looks in azimuth to produce a $\sim 30 \times 30$ m square pixel, geometrical coregistration (Sansosti et al., 2006), fine azimuth coregistration using enhanced spectral diversity (Fattahi et al., 2017), unwrapping using SNAPHU algorithm (Chen & Zebker, 2002), and geocoding and topography correction using a range-doppler geometric approach (Loew & Mauser, 2007; Meier et al., 1993), 30 m SRTM DEM, and real-time (restituted) orbit state vectors. The SLCs are cropped to a 91 km (range) \times 89 km (azimuth) region with the fault at its center.

We derive full 3D displacements, (d_u, d_n, d_e) (Figure 4), from the ascending and descending SAR pixel offsets and the radar imaging geometry. We apply a least squares fit to solve the overdetermined system of equations described in Fialko and Simons (2001):

$$\begin{pmatrix} d_r^{asc} \\ d_r^{dsc} \\ d_{az}^{asc} \\ d_{az}^{dsc} \end{pmatrix} = \begin{pmatrix} -\cos(\theta^{asc}) & -\sin(\theta^{asc}) \sin(\alpha^{asc}) & \sin(\theta^{asc}) \cos(\alpha^{asc}) \\ -\cos(\theta^{dsc}) & -\sin(\theta^{dsc}) \sin(\alpha^{dsc}) & \sin(\theta^{dsc}) \cos(\alpha^{dsc}) \\ 0 & \cos(\alpha^{asc}) & \sin(\alpha^{asc}) \\ 0 & \cos(\alpha^{dsc}) & \sin(\alpha^{dsc}) \end{pmatrix} \begin{pmatrix} d_u \\ d_n \\ d_e \end{pmatrix} \quad (1)$$

where θ is the incidence angle and α is the azimuth of the satellite heading (geographical heading) and d_r and d_{az} is displacement in slant range and azimuth, respectively. The average headings and incidence angles are 350° and 41° for the ascending data and 190° and 39° for the descending data. See Text S1 in Supporting Information S1 for details on the error analysis.

Our GNSS data consists of NGL GPS Coseismic Displacement Rapid 5 min Solutions for both the 6.4 and 7.1 events. We create a cumulative displacement product representing the total 3D surface displacement for shared stations for the Ridgecrest sequence.

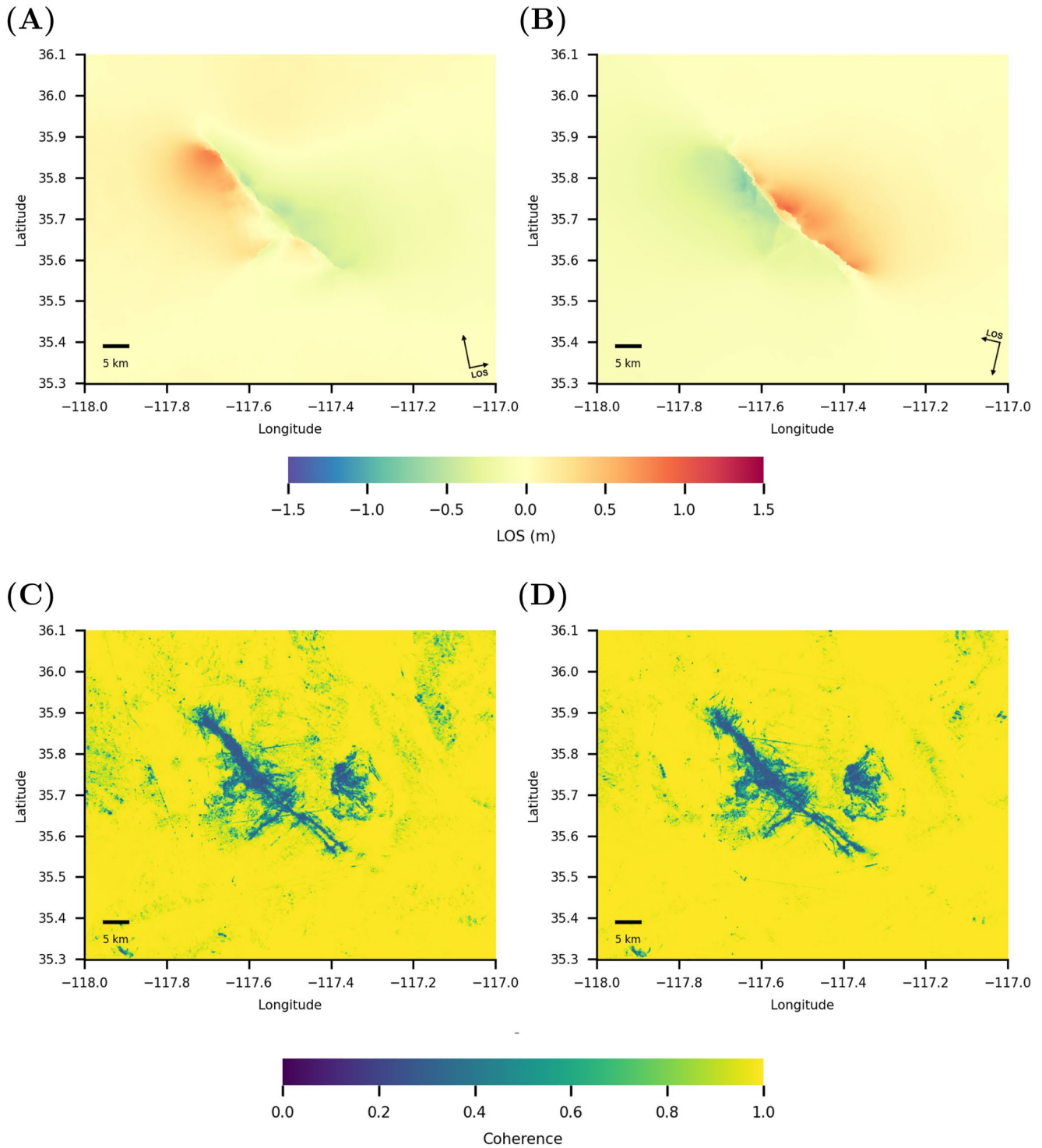


Figure 2. Line of sight displacement images in meters for (a) ascending and (b) descending unwrapped interferograms. Coherence images for (c) ascending and (d) descending interferograms.

3. Methods

In this section we describe our 3D FEM inversion approach to solving for static fault slip and variable rake for the mainshock and foreshock jointly using fused geodetic displacement data.

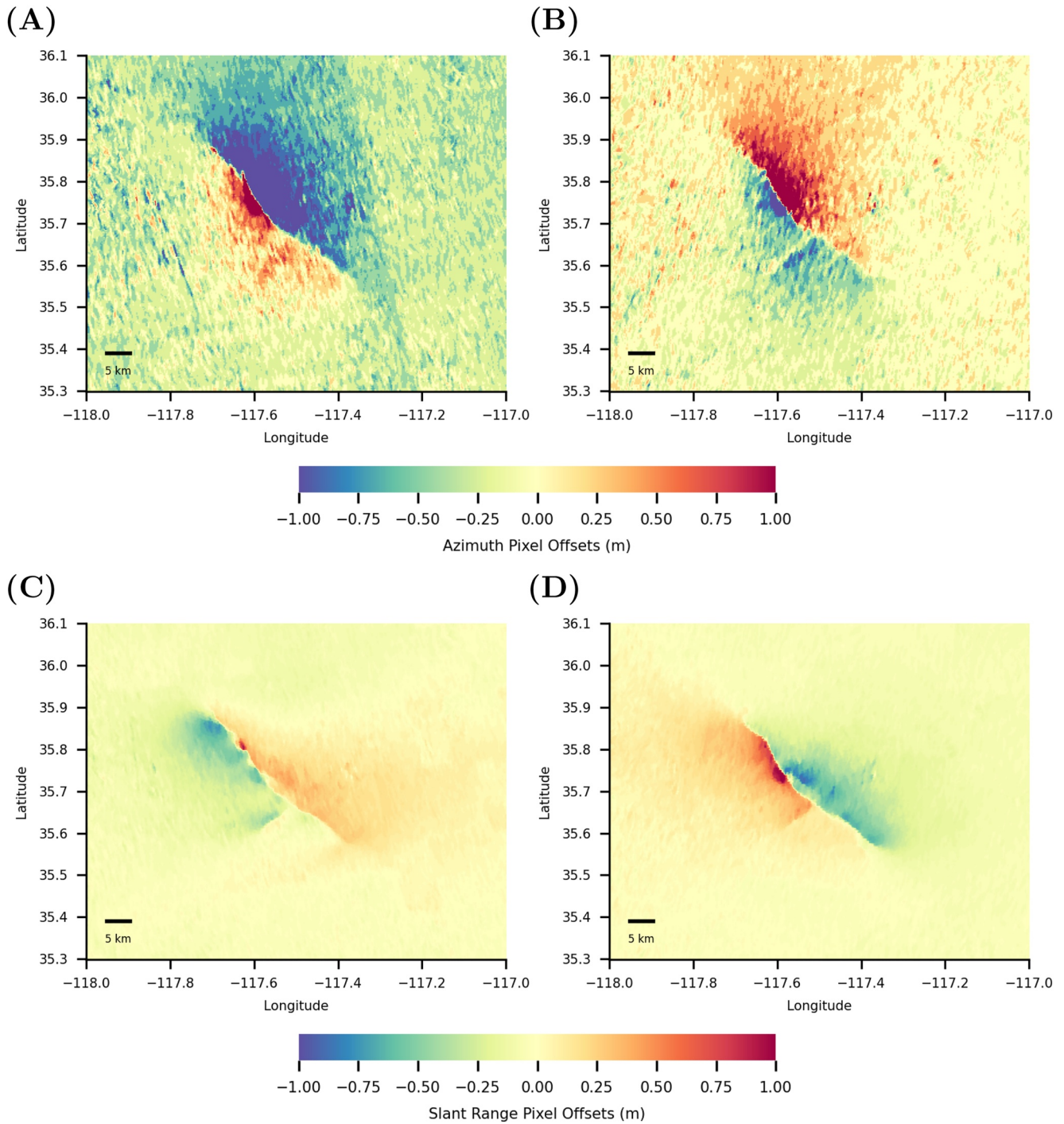


Figure 3. Azimuth pixel offsets in meters for (a) ascending and (b) descending single-look complexes (SLCs). Slant range pixel offsets in meters for (c) ascending and (d) descending SLCs.

3.1. Finite Element Modeling

We construct a 3D mesh representing the earth's structure using the CUBIT meshing software (Blacker et al., 2016). To aid the meshing discretization process, we construct a model consisting of four blocks, a fault block embedded in a near-field block, embedded in an far-field block, overlaying a mantle block (Figure 5). Our model domain is $500 \times 500 \times 500$ km to minimize boundary effects. The origin of our model is the Ridgecrest mainshock epicenter (35.770°N , 117.599°W). We set the near and far-field block thickness to 35 km using the

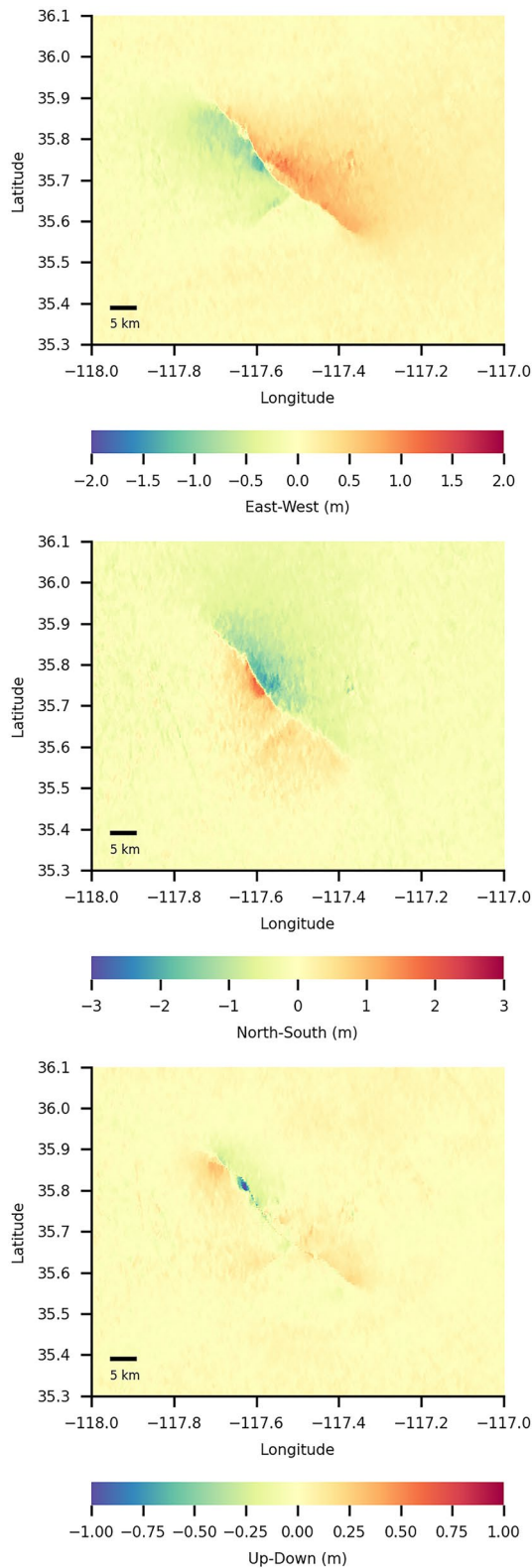


Figure 4. East-west, north-south, and up-down displacements derived from S-1 A/B pixel offsets.

Moho depth from Zhu and Kanamori (2000). We expand the dimensions of the fault block beyond the extent of the fault surface ruptures and the maximum depth of 10 km of the seismogenic zone (Ross et al., 2019) to minimize edge effects (Frey Mueller et al., 1994). Our resulting fault block is 18 km wide, 50 km long, and 22 km high.

In constructing our fault block, we constrain the fault geometry by using smoothed fault surface traces derived from space-based imagery (SCEC Ridgecrest Event Response Page, Mike Oskin) (Figure 6). Our chosen model presented here underwent multiple iterations involving the testing of additional parameters which are explained in detail in Text S1–S7 in Supporting Information S1. The final model features three mainshock fault strands (F1, F2, F3) with an 86° dip and one foreshock fault (F4) with an 66° dip. While we do use a simplified mesh efficiently optimize the dip (Beavan et al., 2012), we believe it is a valid approach since we assume the overall dip solution is not significantly impacted by small wavelength features and localized fault geometry complexities.

We discretize our mesh to varying resolutions to exploit the spatial resolution of the displacement data while maintaining computational feasibility. We control the resolution of our blocks by specifying interval size through a heuristic sizing scheme and by setting the growth factor to 1.3, allowing approximately 30% growth in each layer of adjacent cells. We first apply a meshing resolution of half a kilometer to the top-most surface of the fault block along with a heuristic sizing factor of 4.5 resulting in a mesh density of ~1.5 km in the remainder of the fault block. The discretization of the fault block yields 1,233 split nodes on the surface representing the fault interface. The mesh resolution is incrementally increased by a heuristic sizing factor of 3.5 for the near-field block, seven for the far-field block, and seven for the mantle block, resulting in a resolution of 0.5 km at the fault, ~75 km at the outermost edges of the top of the model, and ~106 km at the bottom of the model. The resulting mesh features a total of 207,075 tetrahedral elements composed of 38,652 total nodes with 6,609 of those nodes at the model surface. CUBIT, by default, optimizes the quality of the mesh by automatically adjusting element connectivity and smoothing. We assess the quality of our final mesh by utilizing CUBIT's condition number metric calculation for tetrahedral elements which reports a reliable mesh quality range of 1.0–7.79.

To evaluate the impact of complex rheology on the inversions, we test two rheology types: (a) a 3D simple elastic structure representing crust-mantle layering, hereinafter referred to as the homogeneous FEM, and (b) a complex rheology using the SCEC Community Velocity Model, hereinafter referred to as heterogeneous FEM. For the homogeneous FEM, the rigidity ($\lambda = \mu$) of the fault, near-field, far-field, and mantle blocks are set to the nominal values of 30, 30, 30, and 70 GPa, respectively (Fialko et al., 2005; Turcotte & Schubert, 2002). For the heterogeneous FEM, we query the SCEC Community Velocity Model (SCEC CVM-S4.26) (Lee et al., 2014; Small et al., 2017) for V_s , V_p , and density values for every node in our mesh. Using these queried values, we compute λ and μ for all 38,652 nodes. For nodes outside the SCEC CVM domain, we assign values of $\lambda = \mu = 70$ GPa if the node depth is deeper than 35 km, and values of $\lambda = \mu = 30$ GPa if the node depth is shallower than 35 km. We calculate the final λ and μ values for all 207,075 elements by averaging the values of its corresponding nodes (Figure 7).

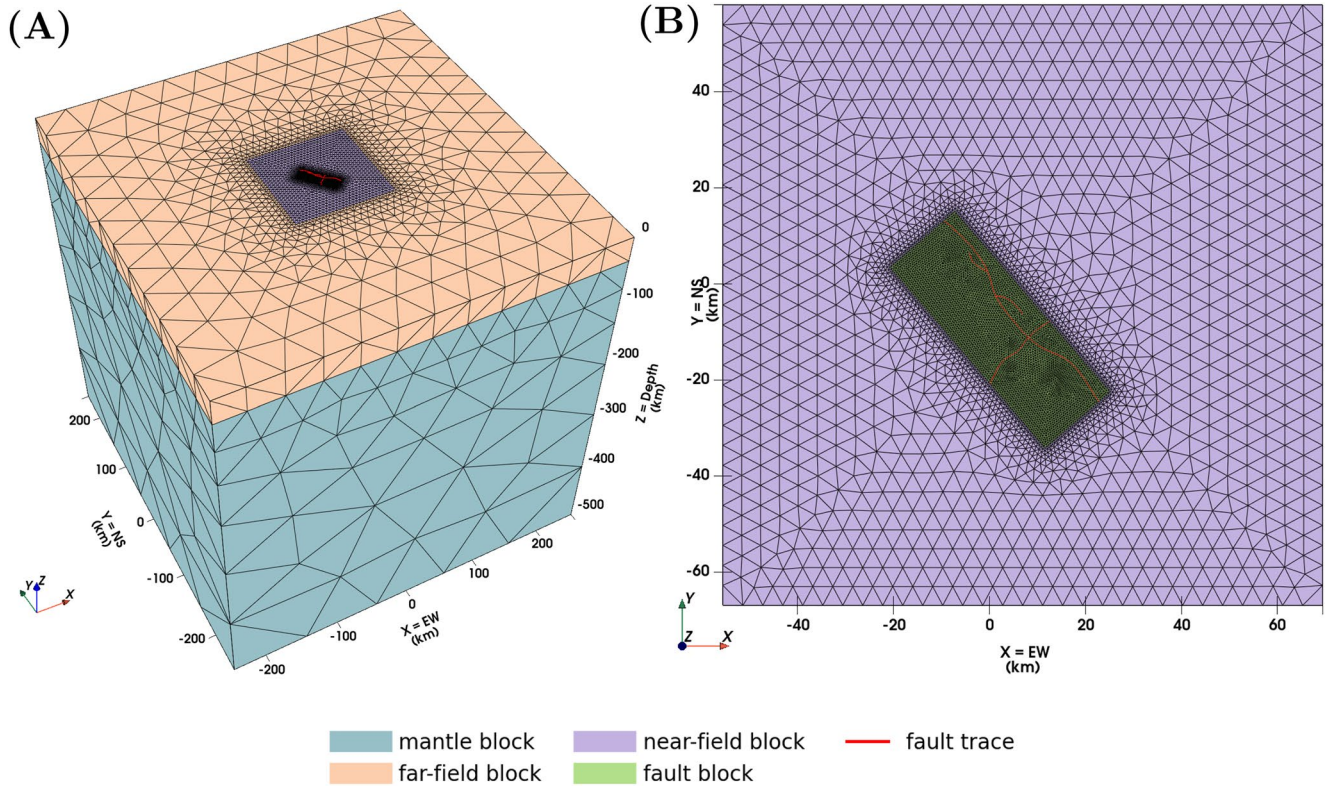


Figure 5. Mesh model blocks in (a) oblique view and (b) top view, zoomed into the near-field and fault blocks. The fault surface trace used in the construction of the fault block is highlighted in red.

3.2. Generating Green's Functions

To solve for slip and variable rake for the Ridgecrest earthquake, we construct Green's function solutions for earthquake displacements by expanding the capabilities of the JPL Geophysical Finite Element Simulation Tool (GeoFEST) software (Parker et al., 2008, 2010). GeoFEST is a simulation system that solves the elliptical partial differential equations (PDE) of elastostatics or viscoelastics. This system of PDEs is subject to boundary conditions such as fault slip dislocation. Fault slip is implemented through split nodes (Melosh & Raefsky, 1981) that define screw or tensile dislocation on the fault without impacting mesh geometry. In the case of elastic earthquake deformation in a 3D domain, GeoFEST models surface displacement given a user defined 3D mesh describing the earth system's fault split nodes and supply Lamé parameters (λ and μ) for isotropic elastic behavior. Instead of

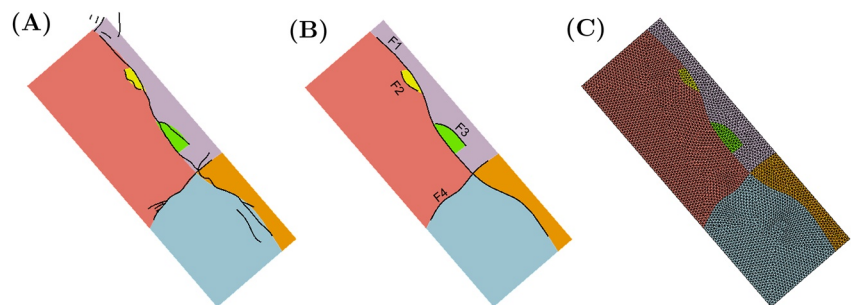


Figure 6. Top view of fault block (a) in solid form overlaid with original fault surface traces (SCEC Ridgecrest Event Response Page, Mike Oskin), (b) in solid form overlaid with smoothed fault surface traces, and (c) in mesh form. The colored blocks represent the final subdivision of the blocks representing fault medium. Fault 1 (F1), the mainshock fault, is represented by surfaces on all the blocks. Fault 2 (F2), the northernmost mainshock subfault, is represented by a surface shared by the pink and yellow blocks. Fault 3 (F3), the southernmost mainshock subfault, is represented by the surface shared by the purple and green blocks. Fault 4 (F4), the foreshock fault, is represented by surfaces on all the blocks.

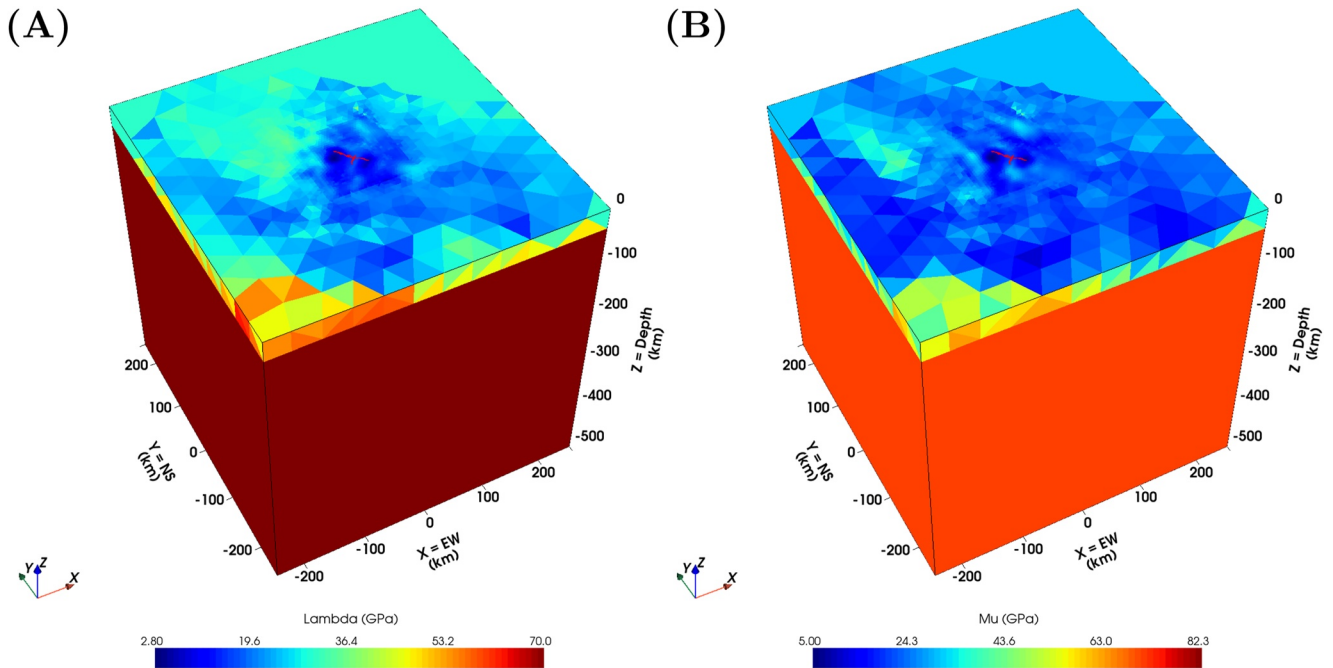


Figure 7. Lamé parameters, (a) λ and (b) μ , for heterogeneous rheology finite element model.

using a single GeoFEST instance to forward model the full displacement field, we run an instance of GeoFEST for each split node in which we assign unit slip to the split node of interest and zero slip to the others to produce numerical displacement Green's functions. Hence, we need two sets of 1,233 Green's functions to model two fault-parallel orientations of slip (strike-parallel and dip-parallel) for each of the 1,233 fault split nodes to enable the inversion to solve for the fault slip magnitude and rake.

3.3. Inversion

We perform a damped, bounded least squares linear inversion to solve for fault slip and rake. We scale our Green's functions matrix and displacement data using data uncertainties and achieve a smooth slip distribution by imposing a Laplacian smoothing operator (Freymueller et al., 1994; Hashima et al., 2016; Jónsson et al., 2002; Maerten et al., 2005). The equation minimized is as follows:

$$F(s, \alpha) = |G's - d'|^2 + \alpha^2 |Ls|^2 \quad (2)$$

where G' is the weighted Green's functions matrix, s is the fault slip array, d' is the weighted 3D surface displacements array, α is the damping parameter, and L is the smoothing operator, also known as the roughness matrix. Weighting is performed using the errors computed from the fused data. We construct L adapting the method in Maerten et al. (2005). We prevent nonphysical retrograde fault slip by constraining our strike-slip and dip-slip bounds from 0 to 7 m. The rake can be made to vary by 90° by estimating linear combinations of Green's functions for the strike-slip component and the dip-slip component. We constrain our mainshock fault rake from -90° to -180° (right-lateral, normal motion) and our foreshock fault rake from 0° to 90° (left-lateral, reverse motion). To determine α , we compute a trade-off curve by plotting variance reduction, Φ , and roughness, ρ , for α values of 0–0.9, in increments of 0.1.

$$\Phi = 1 - \frac{(d - Gs)^T (d - Gs)}{d^T d} \quad (3)$$

$$\rho = (Ls)^T Ls \quad (4)$$

3.4. Geodetic Data Integration

The geodetic data used for the inversion includes differential interferometric synthetic aperture radar (DInSAR) LOS displacements from ascending and descending Sentinel-1 A/B (S1A/B) interferograms, 3D displacements derived from pixel offsets from the ascending and descending S1A/B SLCs, and static GNSS 3D displacements from NGL GPS Coseismic Displacement 5 min Solutions. We incorporate all of the geodetic displacement data by expanding on the DInSAR-GNSS velocity integration method developed by Samsonov and Tiampo (2006) and described thoroughly in Samsonov (2007), Samsonov et al. (2007), Samsonov et al. (2008), and Corsa et al. (2022). The data integration method is based on a Bayesian statistical approach in which an unknown parameter of an energy function is estimated by searching for its minimum (Stan, 2001). The energy function is as follows:

$$U(b/a) = \sum_{i=1}^N \frac{(b_i - a_i)^2}{2\sigma_i^2} \quad (5)$$

$$\begin{aligned} U(d_{LOS}^{asc}, d_{LOS}^{dsc}, d_x^{PO}, d_y^{PO}, d_z^{PO}, d_x^{GNSS}, d_y^{GNSS}, d_z^{GNSS} / d_x, d_y, d_z) = \\ \sum_{i=1}^N C_{LOS}^{asc} (d_{LOS}^{asc} - S_x^{asc} d_x - S_y^{asc} d_y - S_z^{asc} d_z)^2 \\ + C_{LOS}^{dsc} (d_{LOS}^{dsc} - S_x^{dsc} d_x - S_y^{dsc} d_y - S_z^{dsc} d_z)^2 \\ + C_x^{PO} (d_x^{PO} - d_x)^2 + C_y^{PO} (d_y^{PO} - d_y)^2 + C_z^{PO} (d_z^{PO} - d_z)^2 \\ + C_x^{GNSS} (d_x^{GNSS} - d_x)^2 + C_y^{GNSS} (d_y^{GNSS} - d_y)^2 + C_z^{GNSS} (d_z^{GNSS} - d_z)^2 \end{aligned} \quad (6)$$

with coefficients

$$\begin{aligned} C_{LOS}^{asc} &= \frac{1}{2(\sigma_{LOS}^{asc})^2}, & C_{LOS}^{dsc} &= \frac{1}{2(\sigma_{LOS}^{dsc})^2}, \\ C_x^{PO} &= \frac{1}{2(\sigma_x^{PO})^2}, & C_y^{PO} &= \frac{1}{2(\sigma_y^{PO})^2}, & C_z^{PO} &= \frac{1}{2(\sigma_z^{PO})^2}, \\ C_x^{GNSS} &= \frac{1}{2(\sigma_x^{GNSS})^2}, & C_y^{GNSS} &= \frac{1}{2(\sigma_y^{GNSS})^2}, & C_z^{GNSS} &= \frac{1}{2(\sigma_z^{GNSS})^2} \end{aligned} \quad (7)$$

where σ is the standard deviation for the measurements, d_{LOS}^{asc} and d_{LOS}^{dsc} are the interferogram LOS displacements, $[S_x^{asc}, S_y^{asc}, S_z^{asc}]$ and $[S_x^{dsc}, S_y^{dsc}, S_z^{dsc}]$ are the unit vectors pointing from the ground to the satellite, $[d_x^{PO}, d_y^{PO}, d_z^{PO}]$ are the 3D displacements from SAR pixel offsets, and $[d_x^{GNSS}, d_y^{GNSS}, d_z^{GNSS}]$ are 3D GNSS displacements. For a detailed explanation of the method and the error computation of the integrated measurements, see Text S1–S7 in Supporting Information S1. We consider the decoherence in the fault near-field region of the interferograms by disregarding displacements in nodes with coherence values less than 0.4. Figure 8 shows the data combinations used for the inversion for individual nodes.

4. Results

We investigate the impact of the geodetic data source and rheological complexity on the inversion performance by comparing six inversion types. The first three inversion types share the homogeneous rheology but differ in geodetic data source. The first inversion type, henceforth named PO inversion, only utilizes the 3D displacements derived from the pixel offsets. The second inversion type, henceforth named PO_ASC_DSC inversion, uses the 3D displacements resulting from the integrated ascending and descending DInSAR with the pixel offsets. The third inversion type, henceforth named PO_ASC_DSC_GNSS inversion, uses the 3D displacements resulting from the integrated ascending and descending DInSAR with the pixel offsets and GNSS data. Similarly, the remaining three inversions also differ in the geodetic data source but share the heterogeneous rheology type.

Table 2 illustrates how integrating the data reduces the mean sigma of the datasets. Fusing the ascending and descending interferograms with the pixel offsets has the largest impact in x direction, followed by the z direction, and then the y direction. Fusing the GNSS data with the interferograms and pixel offsets does not impact the final fused data sigmas.

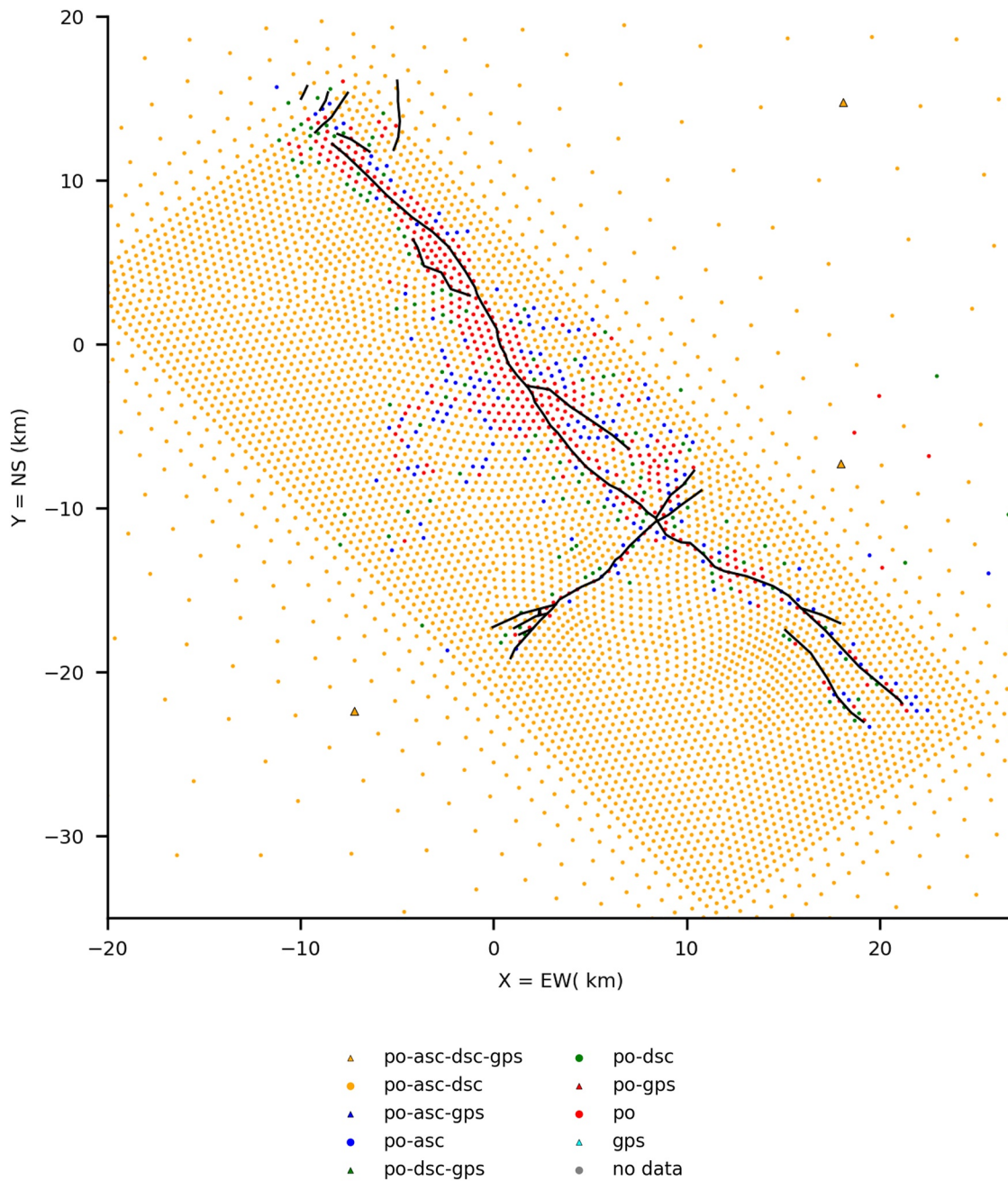


Figure 8. Model surface node plot of data types used for fused data PO_ASC_DSC_GNSS inversion.

Table 2
Sigmas for Pixel Offset Data and Integrated Data

Data	σ_x	σ_y	σ_z
PO	0.06	0.14	0.04
PO_ASC_DSC	0.03	0.13	0.02
PO_ASC_DSC_GNSS	0.03	0.13	0.02

Note. PO, Pixel offsets; ASC, Ascending interferogram; DSC Descending interferogram.

We derive lateral displacements from fault transects 3 km in length and in half kilometer intervals along the primary mainshock fault segment (F1) and the foreshock fault (F4). Figure 9 shows how the PO observations result in larger lateral displacements near the mainshock where maximum lateral slip occurs while the PO_ASC_DSC and PO_ASC_DSC_GNSS observations result in larger displacements at the ends of the mainshock fault rupture. The PO observations result in larger lateral displacements for the overall foreshock fault.

We compute the trade-off curves for the six inversion types. The trade-off curves (see Text S1–S7 in Supporting Information S1) indicate the preferred

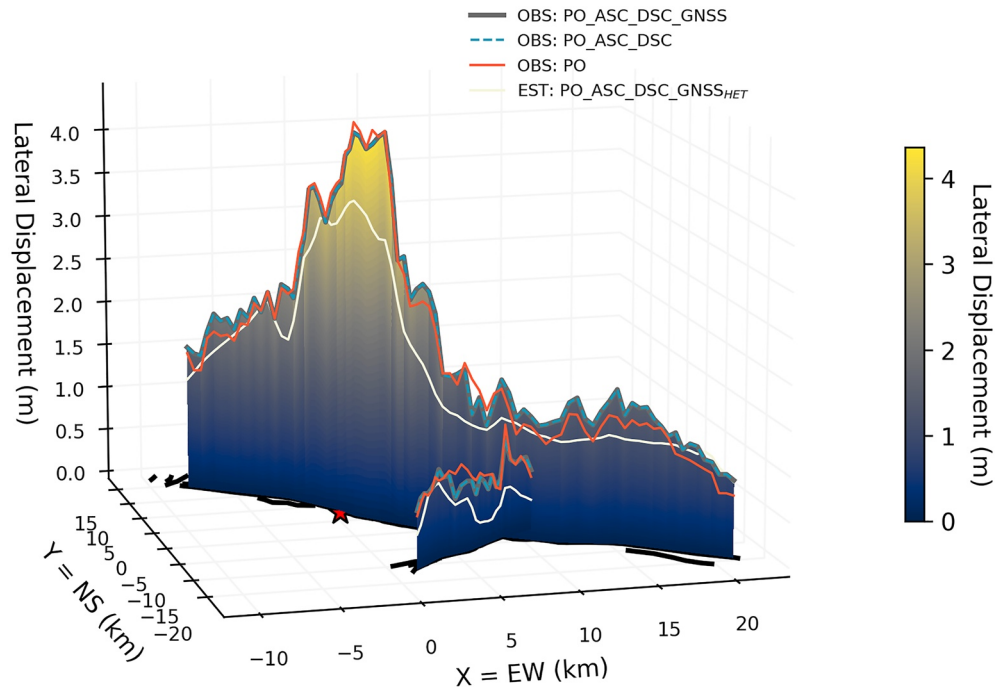


Figure 9. Lateral displacements derived from pixel-offsets (PO), fused PO_ASC_DSC, and fused PO_ASC_DSC_GNSS observations and our preferred model, PO_ASC_DSC_GNSS_{HET}. Also plotted are the mainshock epicenter (red star) and surface fault rupture (heavy black line).

α is 0.2 for PO_{HOM} and PO_{HET} and 0.3 for PO_ASC_DSC_{HOM}, PO_ASC_DSC_{HET}, PO_ASC_DSC_GNSS_{HOM}, and PO_ASC_DSC_GNSS_{HET}.

The average rake and its standard deviation is computed for the nodes with half meter of net-slip or greater (Table 4). In all inversions, the mainshock faults exhibit right-lateral slip with a normal component while the foreshock fault exhibits left-lateral slip with a reverse component (Figure 10). The mainshock secondary fault strands (F2, F3) have a larger normal component compared to the primary mainshock strand (F1). The inversion type that exhibits the highest maximum slip is PO_{HOM}, with a maximum slip of 8.9 m on the northernmost secondary fault strand (F2), at a shallow depth of 2 km. The other homogeneous FEM inversions result in a maximum slip of 6.9 m over two localized regions on the mainshock fault strand (F1), at depths of 2–10 km. For all heterogeneous FEM inversions, the maximum slip of 7.2–7.4 m occurs on the northernmost mainshock secondary fault strand (F2) at a depth of 4 km. All of the inversions show a region of high slip below the mainshock hypocenter at 18 km depth. The spatial extent of this deep slip decreases with the inclusion of additional geodetic data and is the least apparent in PO_ASC_DSC_GNSS_{HET}. For the foreshock fault (F4), the highest slip occurs at its SW edge. All inversions have 6.9 m of maximum slip between 7 and 15 km. The homogeneous FEM inversions show a smoother foreshock slip distribution compared to the heterogeneous FEM inversions. It is worth noting that the PO inversions show edge effects at depth for all faults while the PO_ASC_DSC and PO_ASC_DSC_GNSS inversions only show significant edge effects at depth for the foreshock fault (F4).

Of the six inversion types, PO_{HOM} and PO_{HET} have the poorest fit, with a variance reduction of 7% less than the other inversion types (Table 3). PO_ASC_DSC_{HOM} and PO_ASC_DSC_GNSS_{HOM} have the best fit with a variance reduction at 94.9% followed by PO_ASC_DSC_{HET} and PO_ASC_DSC_GNSS_{HET} at 94.8%.

Our favored model is the PO_ASC_DSC_GNSS_{HET} model (Figure 11) with a smoothing factor, alpha, of 0.3 bounded by 7 m of strike and dip slip, which simulates the overall observed displacement well, featuring a variance reduction of 95% (Figure 12). The randomly scattered, low amplitude residuals, including those in the near-field, support the validity of our model. A small bias from orbit error and atmospheric effects is not detectable in the residuals, and is therefore neglected. The majority of the variance is localized within a kilometer of the fault where our optimal slip model deviates from the observations by 2.2 m in the north-south direction, 0.9 m in the east-west direction, and 0.6 m in the vertical direction.

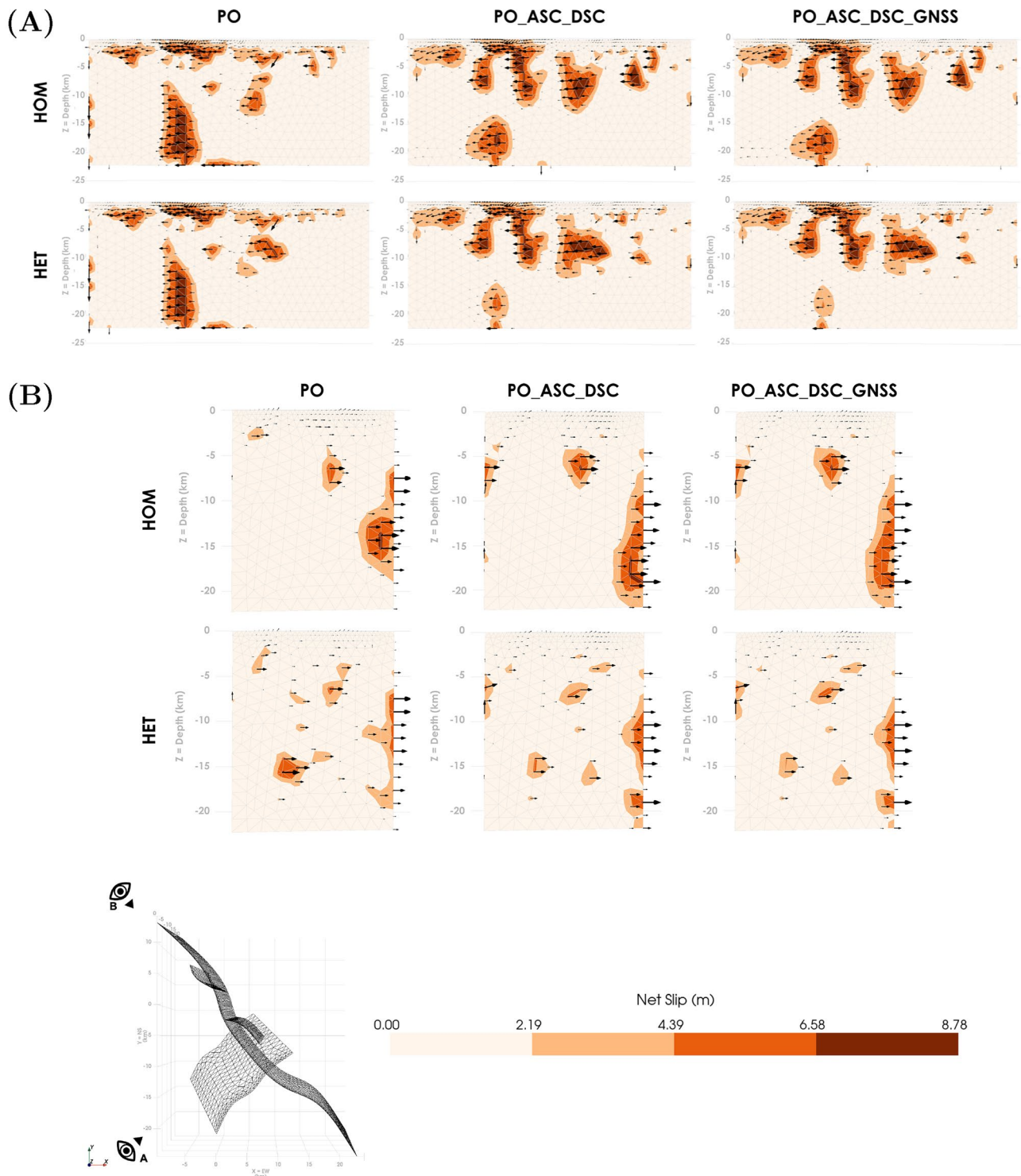


Figure 10. Derived fault slip distributions for (a) mainshock (F1) and (b) foreshock (F4) faults. Bottom left figure is a bird's eye view of the faults showing the approximate vantage points for NE (F1) and SE (F4) viewing perspectives of the faults.

Table 3
Inversion Results

Data	Alpha	Variance reduction (Φ)	Roughness (ρ)
PO _{HOM}	0.2	87.7%	3,760
PO _{HET}	0.2	87.5%	3,862
PO_ASC_DSC _{HOM}	0.3	94.9%	2,279
PO_ASC_DSC _{HET}	0.3	94.8%	2,383
PO_ASC_DSC_GNSS _{HOM}	0.3	94.9%	2,281
PO_ASC_DSC_GNSS _{HET}	0.3	94.8%	2,387

Note. PO, Pixel offsets; ASC, Ascending interferogram; DSC, Descending interferogram; HOM, Homogeneous rheology; HET, Heterogeneous rheology.

Although PO_ASC_DSC_GNSS_{HET} has a lower variance reduction relative to PO_ASC_DSC_GNSS_{HOM} (94.8% vs. 94.9%), we favor the PO_ASC_DSC_GNSS_{HET} model because it results in moment magnitudes more closely corresponding to those obtained using seismic data. The resulting moment magnitudes, assuming a constant shear modulus of 30 GPa, are 8.09 and 7.66 for the mainshock and foreshock of the PO_ASC_DSC_GNSS_{HET} model and 8.12 and 7.69 for the mainshock and foreshock of the PO_ASC_DSC_GNSS_{HOM} model. The resulting moment magnitudes, assuming a variable shear modulus are 7.10 and 6.67 for the mainshock and foreshock of the PO_ASC_DSC_GNSS_{HET} model and 7.13 and 6.70 for the mainshock and foreshock of the PO_ASC_DSC_GNSS_{HOM} model.

The PO_ASC_DSC_GNSS inversions resulted in the mainshock fault strands having a greater dextral component than normal component compared to the PO inversion for the mainshock fault strands (F1, F2, F3). Inversely, the foreshock fault strand (F4) showed average slip closer to sinistral slip than oblique slip in the PO_ASC_DSC_GNSS inversion.

The PO_ASC_DSC_GNSS and PO_ASC_DSC inversions result in a lower rake standard deviation for all the mainshock fault strands, indicating that the mainshock slip model is better constrained relative to the PO inversion.

In terms of computational time, computing a complete set of Green's functions took approximately 9.5 hr on a machine with a 16 GB of RAM and a 2.5 GHz Intel dual-core i7 processor. The Green's functions only need to be computed once for each rheology type and are used for all subsequent inversions. Once all Greens's functions (strike-slip and dip-slip) are computed, the inversion itself takes approximately 4 hr.

5. Discussion

5.1. Observations

To evaluate how well our geodetic data observations represent ground-based field observations, we compare lateral displacements for the various data types (Figure 9) to the cumulative mean-displacement curves in Duross et al. (2020). Our geodetic data observations and ground-based field observations both exhibit maximum lateral displacements of 4+ meters near the mainshock. The cumulative mean-displacement curves in Duross et al. (2020) show a peak right-lateral displacement of 4+ meters in the same approximate location as our peak of 4.4 m. Similarly, the peak left-lateral displacement of 0.7 m is located in the same region as our peak of 1.1 m.

Our mean right-lateral displacement is 2.2 m compared to Duross et al. (2020)'s 1.2 m. Our mean left-lateral displacement is 0.8 m compared to Duross et al. (2020)'s 0.3 m. Our PO_ASC_DSC and PO_ASC_DSC_GNSS geodetic observation sources also show the double-peak foreshock displacement distribution observed in Duross et al. (2020), with the highest peak closest to the primary mainshock fault.

Along the southernmost end of the mainshock fault, both also show lateral displacements between 1 and 1.5 m. Our geodetic data observations overestimate the field observations by 0.5–1.5 m at the northwestern end of the mainshock fault. This discrepancy initiates at the right-step north of the mainshock epicenter and continues northward.

Our geodetic data observations cannot replicate the highest displacements (5+ meters) observed in the field partly due to the sampling our pixel offsets. Our near-field pixel offset displacements are not point measurements, but a representation of average displacement over half a kilometer. This is in agreement with 3 m sampled Planet Labs offsets (Milliner & Donnellan, 2020) which also underestimate the ground-based displacements. WorldView and Pleiades pixel offsets, sampled at half a meter, successfully capture and even exceed the highest field observations (Antoine et al., 2021).

Table 4
Average Inverted Rake and Standard Deviations for Homogeneous and Heterogeneous Rheology Finite Element Model Fault Strands

	PO _{HOM}	PO_ASC_DSC _{HOM}	PO_ASC_DSC_GNSS _{HOM}
F1	-173 ± 20	-175 ± 16	-175 ± 16
F2	-157 ± 34	-172 ± 16	-171 ± 16
F3	-153 ± 37	-173 ± 13	-172 ± 14
F4	7 ± 17	10 ± 23	10 ± 23
	PO _{HET}	PO_ASC_DSC _{HET}	PO_ASC_DSC_GNSS _{HET}
F1	-172 ± 21	-175 ± 15	-175 ± 15
F2	-156 ± 35	-170 ± 18	-170 ± 19
F3	-158 ± 33	-174 ± 12	-174 ± 12
F4	7 ± 19	9 ± 22	9 ± 22

Note. PO, Pixel offsets; ASC, Ascending interferogram; DSC, Descending interferogram.

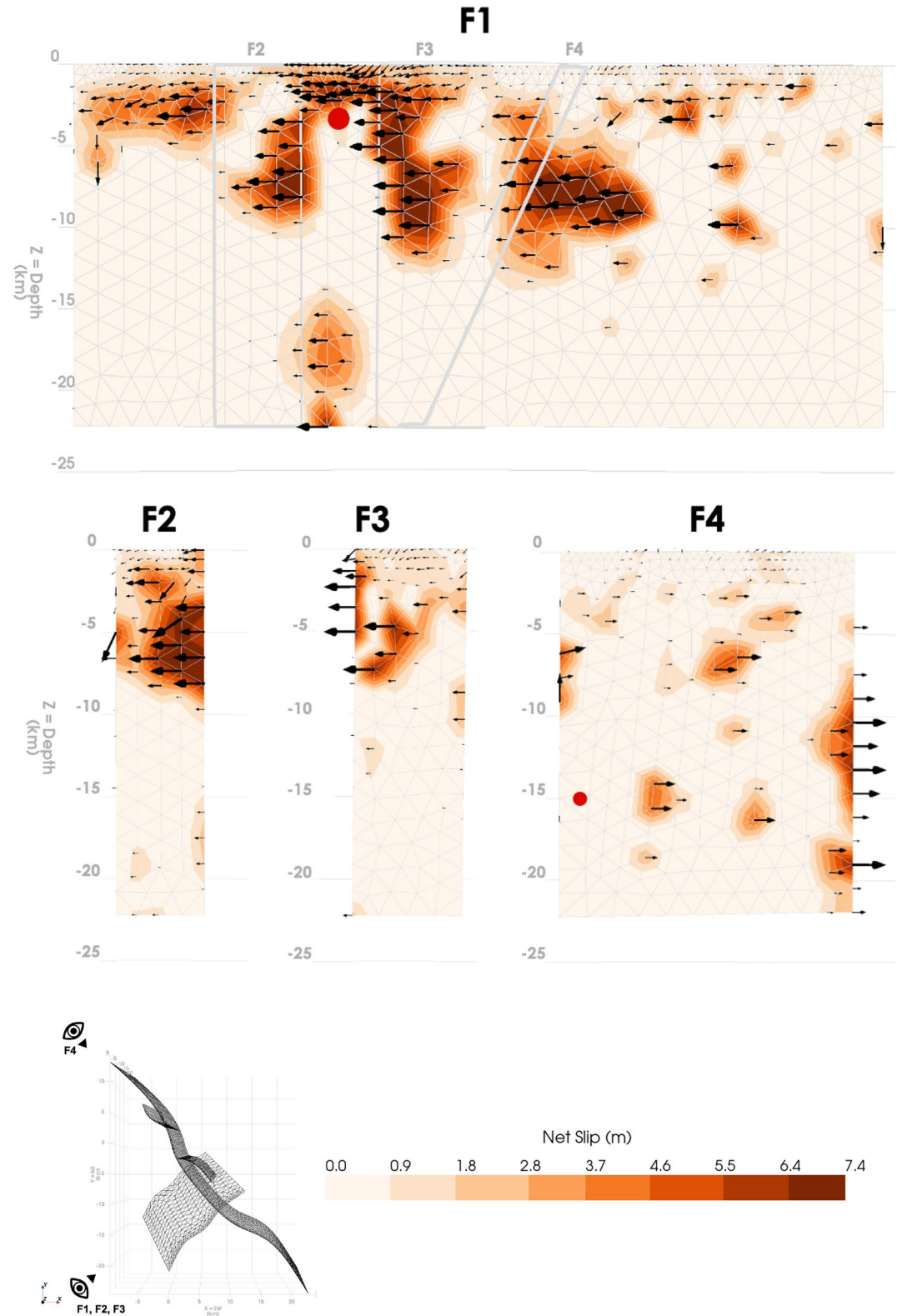


Figure 11. Derived preferred fault slip distribution, $PO_ASC_DSC_GNSS_{HET}$ for mainshock (F1, F2, F3) and foreshock (F4) faults. Bottom left figure is a bird's eye view of the faults showing the approximate vantage points for NE (F1, F2, F3) and SE (F4) viewing perspectives of the faults. Also plotted are the projected relocated hypocenters for the mainshock and foreshock events from Shelly (2020).

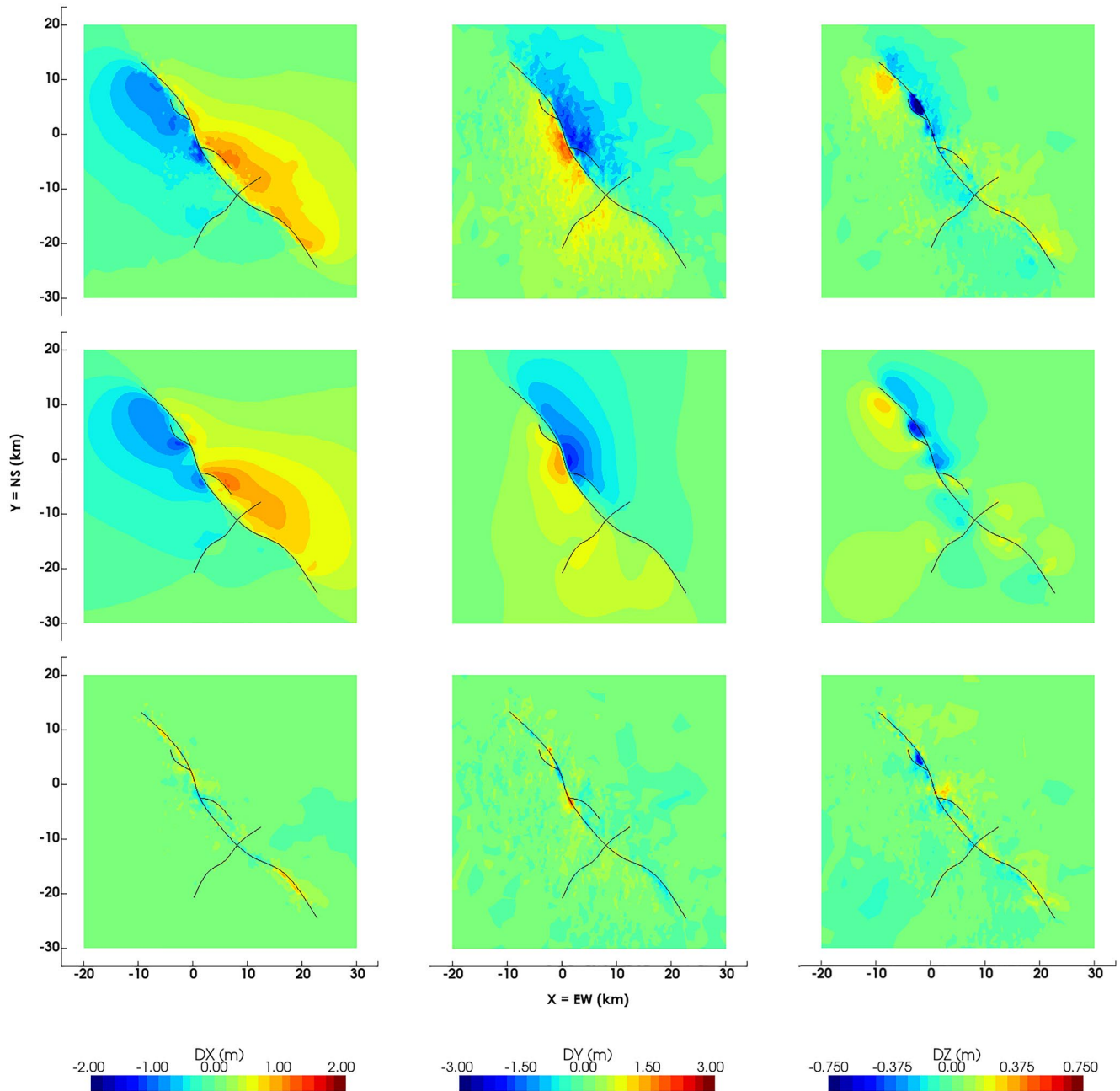


Figure 12. XY mesh plane near-field view of 3D displacement observations (top), model estimates (middle), and residuals (bottom) for our preferred model, $PO_ASC_DSC_GNSS_{HET}$. Our preferred model uses the heterogeneous rheology and the fused observations derived from pixel offsets, interferograms, and GNSS data. Overlaid are the surface traces of our fault model.

5.2. Model Comparisons

We assess the impact of complex rheology and alternative geodetic data sources on the FEM inversion by analyzing variations in the inverted net slip distributions (Figures 13 and 14). A noteworthy feature in Figure 13 is the consistency of the scale, magnitude, and location of the variabilities when comparing rheology models across the three data types. The similarities suggest the rheology is largely responsible for these small wavelength variations, which is intrinsic to complex rheology. Small differences in variations across the data types are observed near the mainshock hypocenter for $PO_{HET-HOM}$ versus $PO_ASC_DSC_{HET-HOM}$ and $PO_{HET-HOM}$ versus $PO_ASC_DSC_GNSS_{HET-HOM}$. Larger wavelength differences in variations for $PO_ASC_DSC_{HET-HOM}$ and

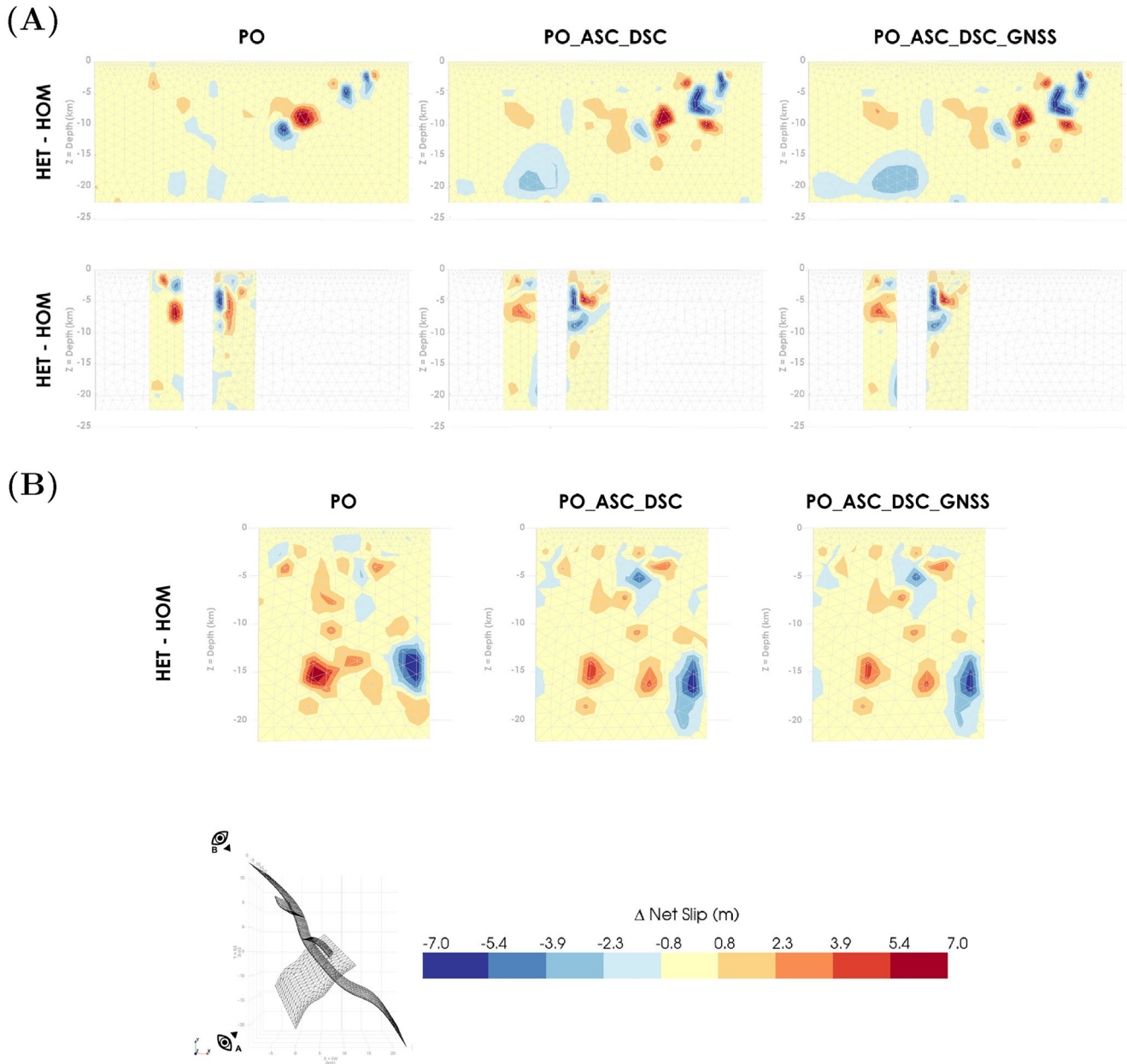


Figure 13. Heterogeneous and homogeneous finite element model variability in derived fault slip distributions for (a) mainshock and (b) foreshock faults. Bottom left figure is a bird's eye view of the faults showing the approximate vantage points for (a) NE and (b) SE viewing perspectives of the faults.

$PO_ASC_DSC_GNSS_{HET-HOM}$ are observed at depths below 15 km Figure 14 highlights variations in the inverted net slip between our preferred model, $PO_ASC_DSC_GNSS_{HET}$ and the other heterogeneous models, PO_{HET} and $PO_ASC_DSC_{HET}$. Significant large scale variations are visible between our preferred model and PO_{HET} . Large scale, but less significant variations are observed between our preferred model and $PO_ASC_DSC_{HET}$ at depths below 10 km for the mainshock faults and at a depth of 5 km for the foreshock fault.

Edge effects for all of mainshock faults are more apparent in the PO inversions compared to the PO_ASC_DSC and $PO_ASC_DSC_GNSS$ inversions (Figure 10). This, along with the aforementioned slip variations at depth observed for PO_{HET} versus $PO_ASC_DSC_{HET}$ and $PO_ASC_DSC_GNSS_{HET}$ (Figure 14), suggest the ascending and descending LOS DInSAR displacements constrained the far-field observations, reducing edge effects resulting from the model's inability to estimate the complete deformation field using short-wavelength displacement measurements. Furthermore, the slip variations observed for $PO_ASC_DSC_{HET}$ versus $PO_ASC_DSC_GNSS_{HET}$ (Figure 14)

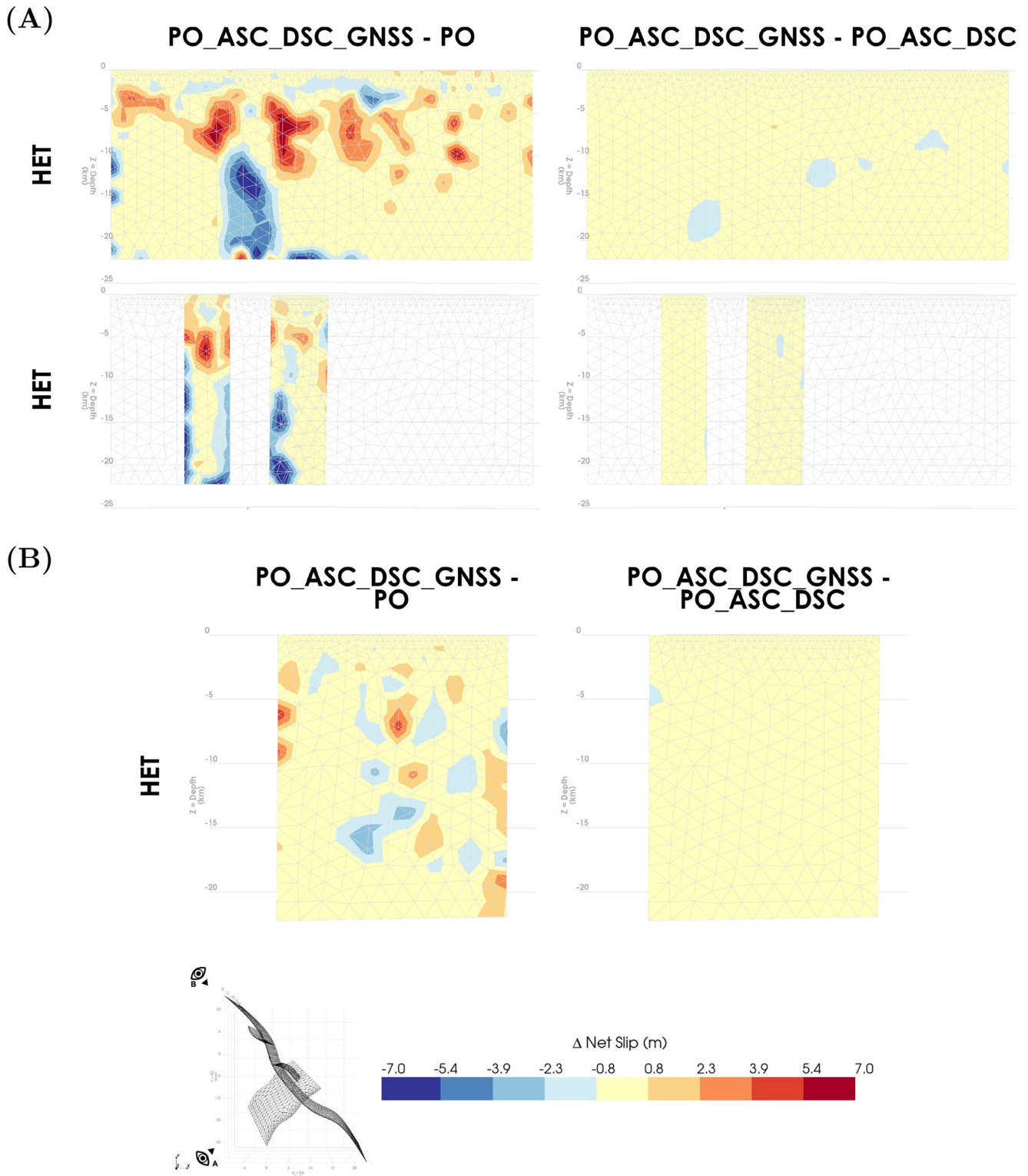


Figure 14. Fault slip distribution difference between preferred model, $PO_ASC_DSC_GNSS_{HET}$, and PO_{HET} and $PO_ASC_DSC_{HET}$ for (a) mainshock and (b) foreshock faults. Bottom left figure is a bird's eye view of the faults showing the approximate vantage points for (a) NE and (b) SE viewing perspectives of the faults.

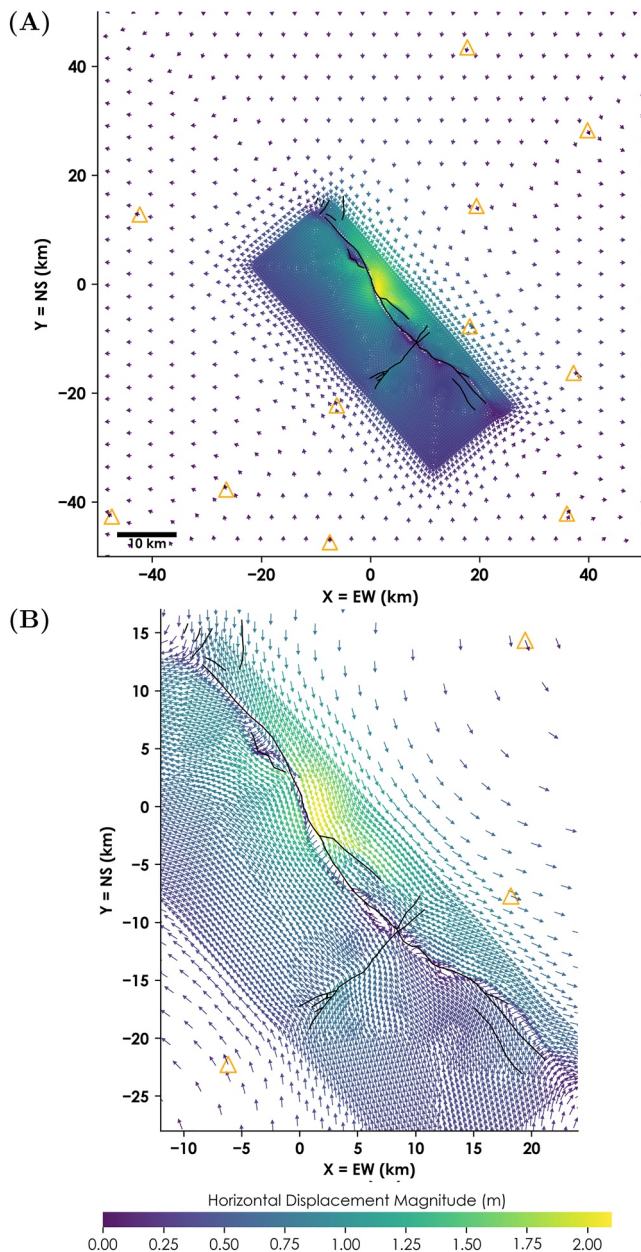


Figure 15. Plots comparing our preferred model's estimated horizontal displacements with those from UNR GPS Coseismic Displacement 5 min Solutions (triangle arrows) for (a) innermost ± 50 km and (b) fault near-field. Arrow direction is direction of horizontal displacement, arrow color is magnitude of horizontal displacement, and arrow length is constant. Overlaid with original fault surface traces (SEEC Ridgecrest Event Response Page, Mike Oskin).

suggest the GNSS displacements further constrained the far-field observations despite the lack of near-field stations and their general sparse coverage for this region. For the foreshock fault (F4), the edge effects are reduced relative to $PO_ASC_DSC_{HET}$ but persist in the $PO_ASC_DSC_{GNSS_{HET}}$ inversion. We attribute this to the overly simplified modeling of this fault strand.

5.3. Preferred Model

Our preferred model is consistent with the UNR GPS Coseismic Displacement 5 min Solutions in the horizontal direction (Figure 15). Assuming a variable shear modulus, we infer geodetic moments of M_w 7.10 and M_w 6.67 for the mainshock and foreshock, respectively. The mainshock geodetic moment coincides with GCMT values while the foreshock geodetic moment is slightly higher. We attribute the discrepancies in the foreshock geodetic moments to the significant edge effects on the west most portion of the fault resulting from the oversimplification of the foreshock fault geometry.

The majority of our preferred model misfit is localized within a kilometer of the fault where our optimal slip model deviates from the observations by 2.2 m in the north-south direction, 0.9 m in the east-west direction, and 0.6 m in the vertical direction (Figure 12). The lateral displacements derived from our preferred model (Figure 9) reach the same maximum value of 2 m observed in the fused $PO_ASC_DSC_{GNSS}$ data just north of the step-over but underestimate the observations by half a meter within the step-over and by a maximum of 1.2 m south of the epicenter where maximum lateral displacement is observed. The near-field misfit potentially can be attributed in part to the smoothing of the fault rupture, resulting in a slight but significant deflection from the original mapped fault surface traces (Figure 6) that coincides with the regions of maximum misfit. Jin and Fialko (2020) attribute similar near-fault misfit to the likely violation of elastic deformation (Fialko et al., 2005; Kaneko & Fialko, 2011; Simons et al., 2002; Xu et al., 2016).

We compare the aftershock density and the slip distribution using the relocated earthquake catalog from Shelly (2020). Figure 16 shows the slip contours are bounded by the mainshock hypocenter and the mainshock aftershocks, as seen by Ross et al. (2019), Tung et al. (2021), and Wetzler et al. (2018). The high density aftershock regions are correlated with regions of a low Poisson's ratio and a high elastic and shear modulus gradient (Figure 17). Past work has shown that gradients in material properties can be considered as additional body forces and thus impact inverted slip magnitude and distribution (Hsu et al., 2011; Williams & Wallace, 2018). The regions of maximum slip are co-located with low and high Poisson's ratio anomalies. The hypocenter is located above an elevated Poisson's ratio and elastic modulus body at 5–8 km depth. This body also appears to perturb the saddle-like fault slip surrounding the hypocenter. The slip perturbation persists in both the heterogeneous and homogeneous $PO_ASC_DSC_{GNSS}$ models (Figure 10). The slip terminates at a depth of 14 km, characterized by a decrease in both the shear modulus and Young's modulus and an increase in Poisson's ratio.

Overall, our foreshock and mainshock slip distribution is confined to the uppermost 10 km, which is in accordance with the maximum depth of the seismogenic zone in this region (Ross et al., 2019).

Our preferred mainshock finite fault model is most similar to that of the model presented in Qiu et al. (2020). Our models both show regions of total slip greater than 7 m, in contrast to the 4–6 m of maximum total slip presented in other studies (Barnhart et al., 2019; Feng et al., 2020; Liu et al., 2019; Magen et al., 2020). Another similarity between the Qiu et al. (2020) model and ours is the deep slip between 15 and 20 km depth below and north of the

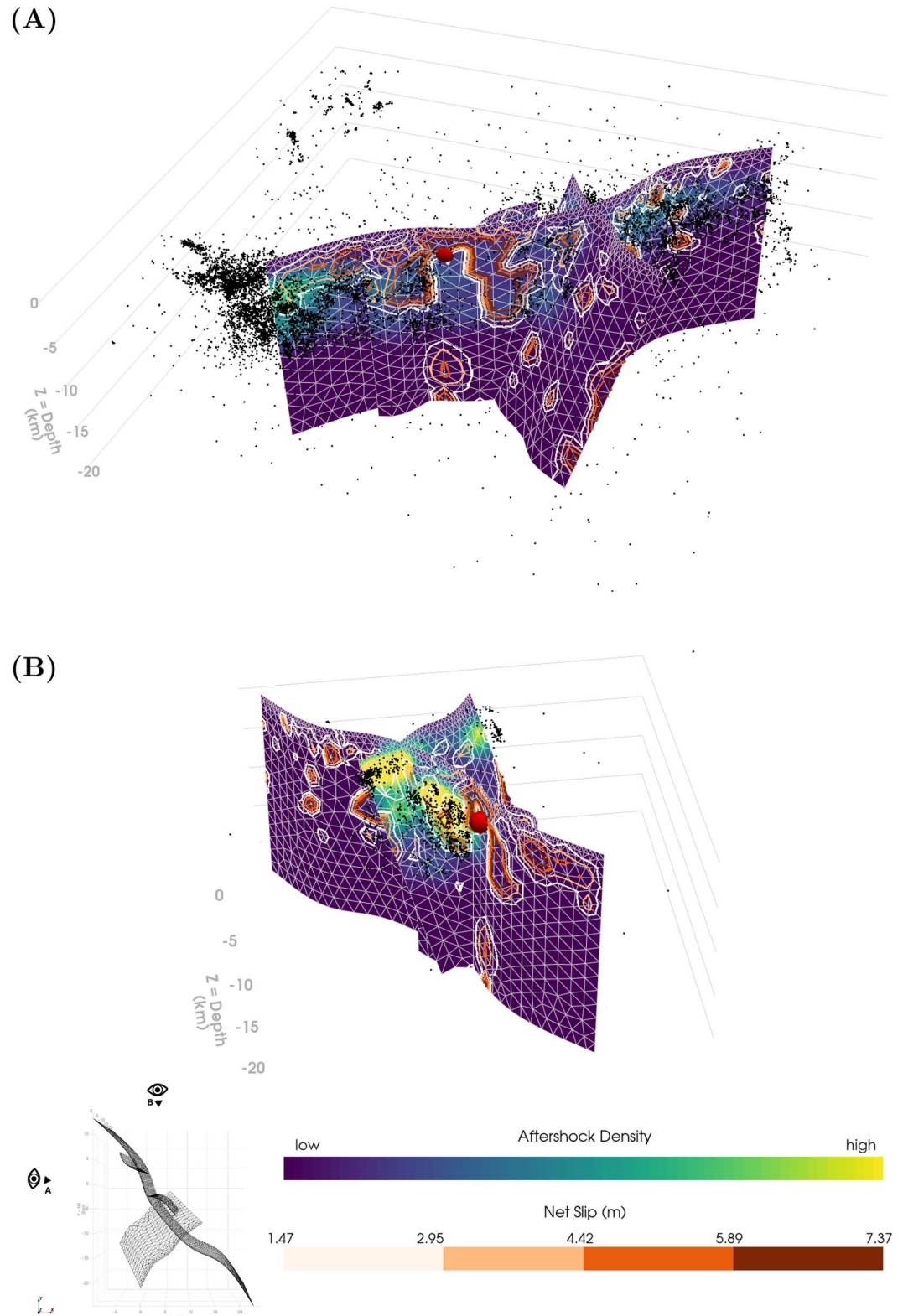


Figure 16. Aftershock density plot of relocated earthquakes above magnitude 1 and shallower than 25 km, overlaid with slip contours for our preferred model, PO_ASC_DSC_GNSS_{HET}. For A, the density plot is comprised of M7.1 aftershocks. For B, the density plot is comprised of M6.4 aftershocks and M7.1 foreshocks. Bottom left figure is a bird's eye view of the faults showing the approximate vantage points for (a) east and (b) south viewing perspectives of the faults. Also plotted are the corresponding relocated hypocenters (Shelly, 2020) as black dots with the relocated mainshock hypocenter as a red sphere.

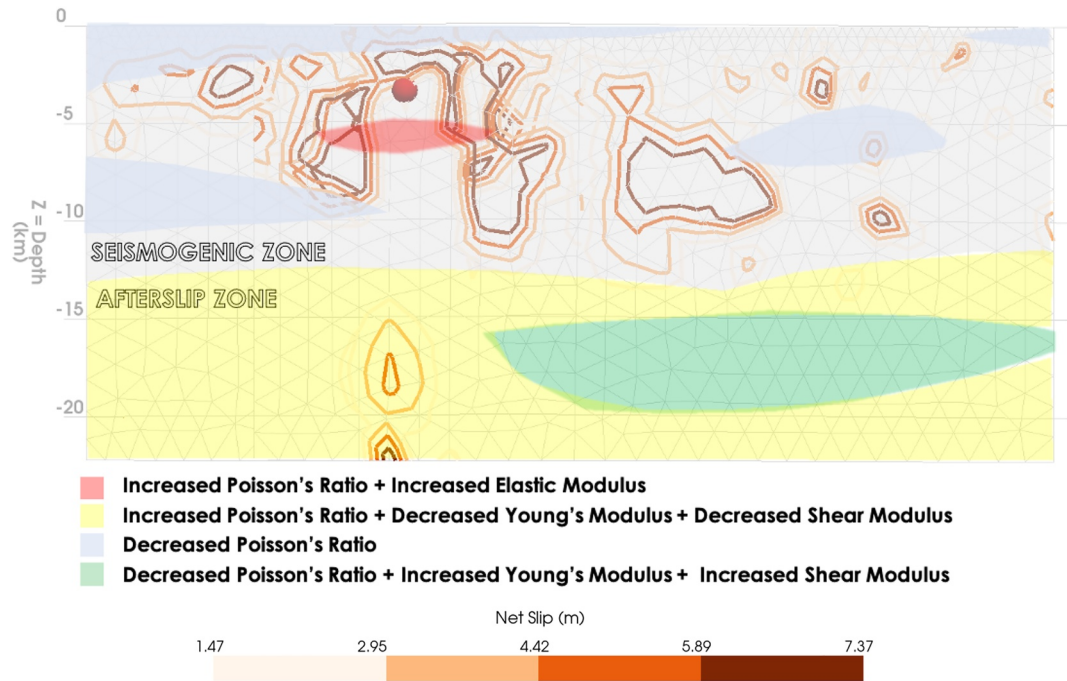


Figure 17. Structural relations overlaid with mainshock slip contours (F1, F2, F3) for our preferred model, PO_ASC_DSC_GNSS_{HET}. Also plotted is the relocated hypocenter for the mainshock event from Shelly (2020).

mainshock. A noteworthy feature present in our preferred model and in Qiu et al. (2020) and Jin and Fialko (2020) is a region of large slip north of the epicenter. The slip of Jin and Fialko (2020) for this region is a maximum of 5 m, while the slip presented in Qiu et al. (2020) more closely resembles the 7+ meters of slip produced in our inversion. Our common use of S1-A/B slant range pixel offsets in the inversion indicates that these near-field observations constrain the localized subsidence associated with the pull-apart basin bounded by F2.

Our preferred model exhibits a significant slip reduction of 37% in the uppermost kilometer, a behavior observed in geodetic slip inversions known as shallow slip deficit (SSD) (Brooks et al., 2017; Fialko et al., 2005; Kaneko & Fialko, 2011; Simons et al., 2002; Wei et al., 2015; Xu et al., 2016). Xu et al. (2016) summarizes the potential sources of SSD as (a) lack of data coverage close to the surface rupture, (b) smoothness regularization, (c) postseismic afterslip, interseismic slip, or triggered slip compensation, and (d) inelastic yielding. Through the inclusion of high-resolution (half kilometer) 3D displacements derived from SAR pixel offsets, we resolve displacements close to the fault rupture to minimize artificial SSD. We compare average slips over one kilometer depth intervals for the primary mainshock for various smoothing factor values, maximum slip bounds, and rheological complexity (see Text S1–S7 in Supporting Information S1). We find that neither varying the smoothing factor, nor changing the maximum slip bounds, nor changing the complexity of rheological parameters impacts the resulting inverted average shallow slip within the uppermost kilometer. Our results strongly suggest SSD observed in the topmost kilometer is likely due to the inability of our elastic model to fully account for the behavior of near-surface materials and associated non-elastic deformation.

6. Conclusions

In this study, we present the application of a high-resolution 3D FEM approach to inverting for fault slip and rake of the 2019 Ridgecrest earthquake sequence. We perform a joint inversion for the mainshock and foreshock events using Sentinel-1 A/B pre- and post-seismic SLCs and coseismic GNSS data. Using the SLCs, we derive coseismic ascending and descending interferograms and pixel offsets. We perform six inversions, half with homogeneous rheology and the other half with complex rheology from the SCEC CVM. For each rheology type, we compare the inversion results for three 3D displacement types: (a) from ascending and descending pixel offsets, (b) from fusing 3D displacements from pixel offsets with ascending and descending interferograms, and (c) from fusing 3D displacements from pixel offsets and GNSS data with ascending and descending pixel offsets.

Our optimal slip model utilizes the fused pixel offsets, interferograms, and GNSS data, along with complex rheology, max slip bounds of 7 m, and a smoothing factor of 0.3. While it is possible to replicate our observations using a smaller smoothing factor (α) and homogeneous rheology, our proposed optimal slip model with a smoothing factor of 0.3 better represents the expected physical behavior of a fault and also more closely replicates the seismically derived moment magnitudes for the event. We acknowledge our model does not replicate the 5+ meters of maximum lateral displacement observed in the field (Duross et al., 2020) and in WorldView and Pleiades optical satellite images (Antoine et al., 2021). Future avenues of research include exploring the impact of the mesh resolution, data sampling, material gradients, and fault complexity on the inverted shallow slip. Future work would also include adding optical imagery and fault rupture estimates into our fused observations to better replicate field measurements.

Although DInSAR LOS displacements decorrelate in the fault's near-field, they provide a valuable contribution to slip inversions in its role in constraining the far-field motion. Pixel offsets provide valuable information on the larger amplitude near-field displacements. Integrated DInSAR LOS displacements and pixel offsets can more accurately capture the displacement of an earthquake in both the near-field and far-field. Our results offer compelling evidence to suggest that for semi-arid regions, the open access Sentinel-1 SLCs can effectively be used for 3D finite fault modeling provided both ascending and descending data acquisitions exist. Similarly, GNSS displacements also play an important role in the inversion. In our inverted slip comparison, we demonstrate that including GNSS data in the fused 3D displacements results in longer wavelength slip variations at depth. We observe that the GNSS displacements further constrained the far-field observations despite the lack of near-field stations and their general sparse coverage for this region. This highlights the need to increase station density in California to improve earthquake characterization. The complete displacement field allows for a comprehensive inversion of the fault slip at all depths.

Our inverted slip is influenced by Poisson's ratio anomaly bodies for both homogeneous and heterogeneous FEMs. Bodies with a decreased Poisson's ratio bound regions of high slip while bodies with an increased Poisson's ratio perturb regions of high slip. Furthermore, we show aftershock deficiency in areas of high coseismic slip, also observed in other studies (Ross et al., 2019; Wetzler et al., 2018). The extent of the majority of our slip is co-located with a 14 km deep feature characterized by a sharp increase in Poisson's ratio and a sharp decrease in Young's modulus and shear modulus which we interpret as the bottom of the seismogenic zone. In comparing inverted slip models, we show that complex rheology introduces small wavelength variations in our inverted slip. Our near-field misfits, which persist in both homogeneous and heterogeneous inversions, suggest that capturing the complex fault geometry has a stronger influence on the inverted solution than rheology when using high-resolution, near-field geodetic data.

In contrast to other studies of this event, our study results in a more complete slip distribution throughout the entire seismogenic zone, uniquely made possible by our efficient FEM approach. We found higher slip values with respect to those reported by Pollitz et al. (2020); Liu et al. (2019); Barnhart et al. (2019); Goldberg et al. (2020); Magen et al. (2020); Jin and Fialko (2020); Wang et al. (2020) and uniquely reproduce a region of localized subsidence. Our SSD analysis suggests the 37% reduction in slip observed in the uppermost kilometer is likely due to our elastic model. We also learn that the maximum slip bounds applied to the geodetic inversion can cause artificial SSD. Once the mesh and observations were finalized, preparing and running the inversion for this high-resolution example took less than 24 hr, including the computation of Green's functions. Once the Green's functions are computed, updating the inversion is accomplished in a matter of hours. The FEM inversion method allows new geodetic data to be easily incorporated without having to recompute the Green's functions. In conclusion, our high-resolution FEM approach utilizing complex fault geometry, complex rheology, and the open access Sentinel-1 SLCs and GNSS data provides an accurate and more detailed characterization of the 2019 Ridgecrest earthquake sequence.

Data Availability Statement

The Sentinel-1 SLCs can be downloaded from the European Space Agency (ESA) Copernicus Open Access Hub (<https://scihub.copernicus.eu/>) and the Alaska Satellite Facility (ASF) Vertex Data Search portal (<https://search.asf.alaska.edu/>). The kmz file of the fault surface traces is available at the SCEC Response Site for the Ridgecrest event (https://response.scec.org/sites/default/files/Ridgecrest%20Surface%20Ruptures_0.kmz). This material is based on services provided by the Geodetic Facility for the Advancement of Geoscience (GAGE)

Facility, operated by UNAVCO, Inc. with support from the National Science Foundation (NSF) and the National Aeronautics and Space Administration (NASA) under NSF Cooperative Agreement EAR-1724794. The Nevada Geodetic Laboratory (NGL) Global Positioning System (GPS) Coseismic Displacement Rapid 5 min Solutions for the Ridgecrest 6.4 and 7.1 events can be downloaded from http://geodesy.unr.edu/news_items/20190705/ci38443183_forweb.txt and http://geodesy.unr.edu/news_items/20190707/ci38457511_forweb.txt, respectively. PyVista software (Sullivan & Kaszynski, 2019) was used for plotting mesh figures. The SCEC Unified Community Velocity Model (UCVM) software (Small et al., 2017) was used to download CVM-S4.26 data. The presented 3D displacement observations and estimations for our mesh surface nodes can be downloaded from the Zenodo data repository (<https://doi.org/10.5281/zenodo.6364437>). Observed data set includes 3D displacements in meters from pixel offsets (PO), from fused pixel offsets, ascending DInSAR, and descending DInSAR (PO_ASC_DSC), and from fused pixel offsets, ascending DInSAR, descending DInSAR, and GNSS (PO_ASC_DSC_GNSS). Estimated data set includes 3D displacements in meters resulting from our final inversions using the aforementioned three data set types for both the homogeneous (HOM) and heterogeneous (HET) rheology types. X , Y , Z coordinate values for node locations are in kilometer distance from Ridgecrest mainshock epicenter (35.770 N, 117.599 W).

Acknowledgments

The authors thank Dr. Mong-Han Huang for invaluable discussions on computing pixel offsets. We also acknowledge Dr. Mike Oskin for the fault surface traces used in constructing our fault geometry and in multiple figures. The authors would like to thank the editor and three reviewers whose comments were essential to improving the manuscript. This study was supported by the National Aeronautics and Space Administration (NASA) Earth Surface and Interior Program (17-ESI-17-0034), Award Number 80NM0018D0004, at the Jet Propulsion Laboratory, California Institute of Technology under a subcontract to the University of Colorado Boulder (Subcontract Number 1602266). It was also supported by the Southern California Earthquake Center (SCEC) (17086, 16147). SCEC is funded by NSF Cooperative Agreement EAR-1600087 and the U.S. Geological Survey (USGS) Cooperative Agreement G17AC00047.

References

- Antoine, S. L., Klinger, Y., Delorme, A., Wang, K., Bürgmann, R., & Gold, R. D. (2021). Diffuse deformation and surface faulting distribution from submetric image correlation along the 2019 Ridgecrest, California, ruptures. *Bulletin of the Seismological Society of America*, *111*(5), 2275–2302. <https://doi.org/10.1785/0120210036>
- Barnhart, W. D., Hayes, G. P., & Gold, R. D. (2019). The July 2019 Ridgecrest, California, earthquake sequence: Kinematics of slip and stressing in cross-fault ruptures. *Geophysical Research Letters*, *46*(21), 11859–11867. <https://doi.org/10.1029/2019GL084741>
- Beavan, J., Motagh, M., Fielding, E. J., Donnelly, N., & Collett, D. (2012). Fault slip models of the 2010–2011 Canterbury, New Zealand, earthquakes from geodetic data and observations of postseismic ground deformation. *New Zealand Journal of Geology and Geophysics*, *55*(3), 207–221. <https://doi.org/10.1080/00288306.2012.697472>
- Blacker, T., Owen, S. J., Staten, M. L., Quadros, R. W., Hanks, B., Clark, B., et al. (2016). CUBIT: Geometry and mesh generation toolkit 15.2 user documentation (No. SAND-2016-1649R). *Sandia National Lab (SNL-NM)*. <https://doi.org/10.2172/1457612>
- Brooks, B. A., Minson, S. E., Glennie, C. L., Nevitt, J. M., Dawson, T., Rubin, R., et al. (2017). Buried shallow fault slip from the South Napa earthquake revealed by near-field geodesy. *Science Advances*, *3*(7), e1700525. <https://doi.org/10.1126/sciadv.1700525>
- Brooks, B. A., Murray, J., Svarc, J., Phillips, E., Turner, R., Murray, M., et al. (2020). Rapid geodetic observations of spatiotemporally varying postseismic deformation following the Ridgecrest earthquake sequence: The U.S. Geological Survey response. *Seismological Research Letters*, *91*(4), 2108–2123. <https://doi.org/10.1785/0220200007>
- Chen, C. W., & Zebker, H. A. (2002). Phase unwrapping for large SAR interferograms: Statistical segmentation and generalized network models. *IEEE Transactions on Geoscience and Remote Sensing*, *40*(8), 1709–1719. <https://doi.org/10.1109/TGRS.2002.802453>
- Chen, K., Avouac, J. P., Aati, S., Milliner, C., Zheng, F., & Shi, C. (2020). Cascading and pulse-like ruptures during the 2019 Ridgecrest earthquakes in the Eastern California Shear Zone. *Nature Communications*, *11*(1), 22. <https://doi.org/10.1038/s41467-019-13750-w>
- Corsa, B., Barba-Sevilla, M., Tiampo, K., & Meertens, C. (2022). Integration of DInSAR time series and GNSS data for continuous volcanic deformation monitoring and eruption early warning applications. *Remote Sensing*, *14*(3), 784. <https://doi.org/10.3390/rs14030784>
- Currenti, G., Negro, C. D., Scandura, D., & Williams, C. A. (2008). Automated procedure for InSAR data inversion using Finite Element Method. In *Proceedings of the 2008 second workshop on use of remote sensing techniques for monitoring volcanoes and seismogenic areas*, (pp.1–5). IEEE. <https://doi.org/10.1109/USEREST.2008.4740336>
- DeMets, C., & Dixon, T. H. (1999). New kinematic models for Pacific-North America motion from 3 Ma to present, I: Evidence for steady motion and biases in the NUVEL-1A model. *Geophysical Research Letters*, *26*(13), 1921–1924. <https://doi.org/10.1029/1999GL900405>
- Dixon, T. H., & Xie, S. (2018). A kinematic model for the evolution of the eastern California shear zone and Garlock fault, Mojave Desert, California. *Earth and Planetary Science Letters*, *494*, 60–68. <https://doi.org/10.1016/j.epsl.2018.04.050>
- Dokka, R. K., & Travis, C. J. (1990). Role of the eastern California shear zone in accommodating Pacific-North American plate motion. *Geophysical Research Letters*, *17*(9), 1323–1326. <https://doi.org/10.1029/GL017i009p01323>
- Donnellan, A., Lyzenga, G., Ansar, A., Goulet, C., Wang, J., & Pierce, M. (2020). Targeted high-resolution structure from motion observations over the M_w 6.4 and 7.1 ruptures of the Ridgecrest earthquake sequence. *Seismological Research Letters*, *91*(4), 2087–2095. <https://doi.org/10.1785/0220190274>
- Duross, C. B., Gold, R. D., Dawson, T. E., Scharer, K. M., Kendrick, K. J., Akciz, S. O., et al. (2020). Surface displacement distributions for the July 2019 Ridgecrest, California, earthquake ruptures. *Bulletin of the Seismological Society of America*, *110*(4), 1400–1418. <https://doi.org/10.1785/0120200058>
- Fattahi, H., Agram, P., & Simons, M. (2017). A network-based enhanced spectral diversity approach for TOPS time-series analysis. *IEEE Transactions on Geoscience and Remote Sensing*, *55*(2), 777–786. <https://doi.org/10.1109/TGRS.2016.2614925>
- Feng, W., Samsonov, S., Qiu, Q., Wang, Y., Zhang, P., Li, T., & Zheng, W. (2020). Orthogonal fault rupture and rapid postseismic deformation following 2019 Ridgecrest, California, earthquake sequence revealed from geodetic observations. *Geophysical Research Letters*, *47*(5), e2019GL086888. <https://doi.org/10.1029/2019GL086888>
- Fialko, Y., Sandwell, D., Simons, M., & Rosen, P. (2005). Three-dimensional deformation caused by the Bam, Iran, earthquake and the origin of shallow slip deficit. *Nature*, *435*(7040), 295–299. <https://doi.org/10.1038/nature03425>
- Fialko, Y., Simons, M., & Agnew, D. (2001). The complete (3-D) surface displacement field in the epicentral area of the 1999 M_w 7.1 Hector Mine earthquake, California from space geodetic observations. *Geophysical Research Letters*, *28*(16), 3063–3066. <https://doi.org/10.1029/2001gl013174>
- Freed, A. M. (2007). Afterslip (and only afterslip) following the 2004 Parkfield, California, earthquake. *Geophysical Research Letters*, *34*(6), L06312. <https://doi.org/10.1029/2006GL029155>

- Frey Mueller, J., King, N. E., & Segall, P. (1994). The co-seismic slip distribution of the Landers earthquake. *Bulletin of the Seismological Society of America*, 84(3), 646–659. <https://doi.org/10.1785/bssa0840030646>
- Goldberg, D. E., Melgar, D., Sahakian, V. J., Thomas, A. M., Xu, X., Crowell, B. W., & Geng, J. (2020). Complex rupture of an immature fault zone: A simultaneous kinematic model of the 2019 Ridgecrest, CA earthquakes. *Geophysical Research Letters*, 47(3). e2019GL086382. <https://doi.org/10.1029/2019GL086382>
- Hashima, A., Becker, T. W., Freed, A. M., Sato, H., & Okaya, D. A. (2016). Coseismic deformation due to the 2011 Tohoku-oki earthquake: Influence of 3-D elastic structure around Japan. *Earth Planets and Space*, 68(1), 159. <https://doi.org/10.1186/s40623-016-0535-9>
- Hauksson, E., Jones, L. M., Hutton, K., & Eberhart-Phillips, D. (1993). The 1992 Landers earthquake sequence: Seismological observations. *Journal of Geophysical Research*, 98(B11), 19835–19858. <https://doi.org/10.1029/93jb02384>
- Hsu, Y. J., Simons, M., Williams, C., & Casarotti, E. (2011). Three-dimensional FEM derived elastic Green's functions for the coseismic deformation of the 2005 M_w 8.7 Nias-Simeulue, Sumatra earthquake. *Geochemistry, Geophysics, Geosystems*, 12(7), 7013. <https://doi.org/10.1029/2011GC003553>
- Hudnut, K. W., Brooks, B. A., Scharer, K., Hernandez, J. L., Dawson, T. E., Oskin, M. E., et al. (2020). Airborne lidar and electro-optical imagery along surface ruptures of the 2019 Ridgecrest earthquake sequence, Southern California. *Seismological Research Letters*, 91(4), 2096–2107. <https://doi.org/10.1785/0220190338>
- Jin, Z., & Fialko, Y. (2020). Finite slip models of the 2019 Ridgecrest earthquake sequence constrained by space geodetic data and aftershock locations. *Bulletin of the Seismological Society of America*, 110(4), 1660–1679. <https://doi.org/10.1785/0120200060>
- Jónsson, S., Zebker, H., Segall, P., & Amelung, F. (2002). Fault slip distribution of the 1999 M_w 7.1 Hector Mine, California, earthquake, estimated from satellite radar and GPS measurements. *Bulletin of the Seismological Society of America*, 92(4), 1377–1389. <https://doi.org/10.1785/0120000922>
- Kaneko, Y., & Fialko, Y. (2011). Shallow slip deficit due to large strike-slip earthquakes in dynamic rupture simulations with elasto-plastic off-fault response. *Geophysical Journal International*, 186(3), 1389–1403. <https://doi.org/10.1111/j.1365-246X.2011.05117.x>
- Lee, E. J., Chen, P., Jordan, T. H., Maechling, P. B., Denolle, M. A., & Beroza, G. C. (2014). Full-3-D tomography for crustal structure in Southern California based on the scattering-integral and the adjoint-wavefield methods. *Journal of Geophysical Research: Solid Earth*, 119(8), 6421–6451. <https://doi.org/10.1002/2014JB011346>
- Liu, C., Lay, T., Brodsky, E. E., Dascher-Cousineau, K., & Xiong, X. (2019). Coseismic rupture process of the large 2019 Ridgecrest earthquakes from joint inversion of geodetic and seismological observations. *Geophysical Research Letters*, 46(21), 11820–11829. <https://doi.org/10.1029/2019GL084949>
- Liu, M., Wang, H., & Li, Q. (2010). Inception of the Eastern California shear zone and evolution of the Pacific-North American plate boundary: From kinematics to geodynamics. *Journal of Geophysical Research*, 115(B7), 7401. <https://doi.org/10.1029/2009jb007055>
- Loew, A., & Mauser, W. (2007). Generation of geometrically and radiometrically terrain corrected SAR image products. *Remote Sensing of Environment*, 106(3), 337–349. <https://doi.org/10.1016/j.rse.2006.09.002>
- Maerten, F., Resor, P., Pollard, D., & Maerten, L. (2005). Inverting for slip on three-dimensional fault surfaces using angular dislocations. *Bulletin of the Seismological Society of America*, 95(5), 1654–1665. <https://doi.org/10.1785/0120030181>
- Magen, Y., Ziv, A., Inbal, A., Baer, G., & Hollingsworth, J. (2020). Fault rerupture during the July 2019 Ridgecrest earthquake pair from joint slip inversion of insar, optical imagery, and gps. *Bulletin of the Seismological Society of America*, 110(4), 1627–1643. <https://doi.org/10.1785/0120200024>
- Masterlark, T. (2003). Finite element model predictions of static deformation from dislocation sources in a subduction zone: Sensitivities to homogeneous, isotropic, Poisson-solid, and half-space assumptions. *Journal of Geophysical Research*, 108(B11), 2540. <https://doi.org/10.1029/2002jb002296>
- Masterlark, T., DeMets, C., Wang, H. F., Sánchez, O., & Stock, J. (2001). Homogeneous vs heterogeneous subduction zone models: Coseismic and postseismic deformation. *Geophysical Research Letters*, 28(21), 4047–4050. <https://doi.org/10.1029/2001GL013612>
- Masterlark, T., & Hughes, K. L. (2008). Next generation of deformation models for the 2004 M9 Sumatra-Andaman earthquake. *Geophysical Research Letters*, 35(19), 19310. <https://doi.org/10.1029/2008GL035198>
- Mattioli, G. S., Phillips, D. A., Hodgkinson, K. M., Walls, C., Mencin, D. J., Bartel, B. A., et al. (2020). The GAGE data and field response to the 2019 Ridgecrest earthquake sequence. *Seismological Research Letters*, 91(4), 2075–2086. <https://doi.org/10.1785/0220190283>
- Meier, E., Frei, U., Nüesch, D., & Schreier, G. (1993). Precise terrain corrected geocoded images. *SAR Geocoding: Data Systems*, 173–185.
- Melgar, D., Melbourne, T. I., Crowell, B. W., Geng, J., Szeliga, W., Scrivner, C., et al. (2019). Real-time high-rate GNSS displacements: Performance demonstration during the 2019 Ridgecrest, California, earthquakes. *Seismological Research Letters*, 91(4), 1943–1951. <https://doi.org/10.1785/0220190223>
- Melosh, H. J., & Raefsky, A. (1981). A simple and efficient method for introducing faults into finite element computations. *Bulletin of the Seismological Society of America*, 71(5), 1391–1400. <https://doi.org/10.1785/bssa0710051391>
- Milliner, C., & Donnellan, A. (2020). Using daily observations from planet labs satellite imagery to separate the surface deformation between the 4 July M_w 6.4 foreshock and 5 July M_w 7.1 mainshock during the 2019 Ridgecrest earthquake sequence. *Seismological Research Letters*, 91(4), 1986–1997. <https://doi.org/10.1785/0220190271>
- Parker, J., Lyzenga, G., Norton, C., Zuffada, C., Glasscoe, M., Lou, J., & Donnellan, A. (2008). Geophysical finite-element simulation tool (GeoFEST): Algorithms and validation for quasistatic regional faulted crust problems. *Pure and Applied Geophysics*, 165(3–4), 497–521. <https://doi.org/10.1007/s00024-008-0325-9>
- Parker, J., Norton, C., & Lyzenga, G. (2010). Parallel GeoFEST for regional faulted deformation. In *Concurrency and computation: Practice and experience* (Vol. 22, pp. 1604–1625). John Wiley & Sons, Ltd. <https://doi.org/10.1002/cpe.1511>
- Pollitz, F. F., Murray, J. R., Svarc, J. L., Wicks, C., Roeloffs, E., Minson, S. E., et al. (2020). Kinematics of fault slip associated with the 4–6 July 2019 Ridgecrest, California, earthquake sequence. *Bulletin of the Seismological Society of America*, 110(4), 1688–1700. <https://doi.org/10.1785/0120200018>
- Ponti, D. J., Blair, J. L., Rosa, C. M., Thomas, K., Pickering, A. J., Akciz, S., et al. (2020). Documentation of surface fault rupture and ground-deformation features produced by the 4 and 5 July 2019 M_w 6.4 and M_w 7.1 Ridgecrest earthquake sequence. *Seismological Research Letters*, 91, 2942–2959. <https://doi.org/10.1785/0220190322>
- Qiu, Q., Barbot, S., Wang, T., & Wei, S. (2020). Slip complementarity and triggering between the foreshock, mainshock, and afterslip of the 2019 Ridgecrest rupture sequence. *Bulletin of the Seismological Society of America*, 110(4), 1701–1715. <https://doi.org/10.1785/0120200037>
- Rosen, P. A., Gurrola, E. M., Franco Sacco, G., & Zebker, H. A. (2012). The InSAR scientific computing environment. In *EUSAR 2012, Proceedings of the 9th European conference on synthetic aperture radar* (pp. 730–733). VDE. Retrieved from https://trs.jpl.nasa.gov/bitstream/handle/2014/43527/11-5426_A1b.pdf?sequence=1

- Ross, Z. E., Idini, B., Jia, Z., Stephenson, O. L., Zhong, M., Wang, X., et al. (2019). Hierarchical interlocked orthogonal faulting in the 2019 Ridgecrest earthquake sequence. *Science*, 366(6463), 346–351. <https://doi.org/10.1126/science.aaz0109>
- Samsonov, S. (2007). Integration of Differential InSAR and GPS measurements for studying of surface deformation (Unpublished doctoral dissertation)
- Samsonov, S., & Tiampo, K. (2006). Analytical optimization of a DInSAR and GPS dataset for derivation of three-dimensional surface motion. *IEEE Geoscience and Remote Sensing Letters*, 3(1), 107–111. <https://doi.org/10.1109/LGRS.2005.858483>
- Samsonov, S., Tiampo, K., Rundle, J., & Li, Z. (2007). Application of DInSAR-GPS optimization for derivation of fine-scale surface motion maps of Southern California. *IEEE Transactions on Geoscience and Remote Sensing*, 45(2), 512–521. <https://doi.org/10.1109/TGRS.2006.887166>
- Samsonov, S. V., Tiampo, K. F., & Rundle, J. B. (2008). Application of DInSAR-GPS optimization for derivation of three-dimensional surface motion of the southern California region along the San Andreas fault. *Computers & Geosciences*, 34(5), 503–514. <https://doi.org/10.1016/j.cageo.2007.05.013>
- Sansosti, E., Berardino, P., Manunta, M., Serafino, F., & Fornaro, G. (2006). Geometrical SAR image registration. *IEEE Transactions on Geoscience and Remote Sensing*, 44(10), 2861–2870. <https://doi.org/10.1109/TGRS.2006.875787>
- Sauber, J., Thatcher, W., & Solomon, S. C. (1986). Geodetic measurement of deformation in the central Mojave Desert, California. *Journal of Geophysical Research*, 91(B12), 12683–12693. <https://doi.org/10.1029/jb091ib12p12683>
- Sauber, J., Thatcher, W., Solomon, S. C., & Lisowski, M. (1994). Geodetic slip rate for the eastern California shear zone and the recurrence time of Mojave Desert earthquakes. *Nature*, 367(6460), 264–266. <https://doi.org/10.1038/367264a0>
- Shelly, D. R. (2020). A high-resolution seismic catalog for the initial 2019 Ridgecrest earthquake sequence: Foreshocks, aftershocks, and faulting complexity. *Seismological Research Letters*, 91(4), 1971–1978. <https://doi.org/10.1785/0220190309>
- Simons, M., Fialko, Y., & Rivera, L. (2002). Coseismic deformation from the 1999 M_w 7.1 Hector Mine, California, earthquake as inferred from InSAR and GPS observations. *Bulletin of the Seismological Society of America*, 92(4), 1390–1402. <https://doi.org/10.1785/0120000933>
- Small, P., Gill, D., Maechling, P. J., Taborda, R., Callaghan, S., Jordan, T. H., et al. (2017). The SCEC unified community velocity model software framework. *Seismological Research Letters*, 88(6), 1539–1552. <https://doi.org/10.1785/0220170082>
- Stan, L. (2001). *Markov random field modeling in image analysis*. Springer.
- Stewart, J. P., Brandenberg, S. J., Wang, P., Nweke, C. C., Hudson, K., Mazzoni, S., et al. (2019). *Preliminary report on engineering and geological effects of the July 2019 Ridgecrest earthquake sequence*. Geotechnical Extreme Event Reconnaissance Association. (pp. 1–69). (Technical Report). <https://doi.org/10.18118/G6H66K>
- Sullivan, C., & Kaszynski, A. (2019). PyVista: 3D plotting and mesh analysis through a streamlined interface for the visualization toolkit (VTK). *Journal of Open Source Software*, 4(37), 1450. <https://doi.org/10.121105/joss.01450>
- Taira, T., & Bent, A. (2020). Preface to the seismological research letters data mine focus section on the 2019 Ridgecrest earthquake sequence. *Seismological Society of America*, 91(4), 1940–1942. <https://doi.org/10.1785/0220200155>
- Takeuchi, C. S., & Fialko, Y. (2013). On the effects of thermally weakened ductile shear zones on postseismic deformation. *Journal of Geophysical Research: Solid Earth*, 118(12), 6295–6310. <https://doi.org/10.1002/2013JB010215>
- Tung, S., & Masterlark, T. (2018). Resolving source geometry of the 24 august 2016 Amatrice, Central Italy, earthquake from in SAR data and 3D finite-element modeling. *Bulletin of the Seismological Society of America*, 108(2), 553–572. <https://doi.org/10.1785/0120170139>
- Tung, S., Shirzaei, M., Ojha, C., Pepe, A., & Liu, Z. (2021). Structural controls over the 2019 Ridgecrest earthquake sequence investigated by high-fidelity elastic models of 3D velocity structures. *Journal of Geophysical Research: Solid Earth*, 126(7). <https://doi.org/10.1029/2020JB021124>
- Turcotte, D. L., & Schubert, G. (2002). *Geodynamics*. Cambridge university press.
- Wang, K., Dreger, D. S., Tinti, E., Bürgmann, R., & Taira, T. (2020). Rupture process of the 2019 Ridgecrest, California M_w 6.4 foreshock and M_w 7.1 earthquake constrained by seismic and geodetic data. *Bulletin of the Seismological Society of America*, 110(4), 1603–1626. <https://doi.org/10.1785/0120200108>
- Wei, S., Barbot, S., Graves, R., Lienkaemper, J. J., Wang, T., Hudnut, K., et al. (2015). The 2014 M_w 6.1 South Napa earthquake: A unilateral rupture with shallow asperity and rapid afterslip. *Seismological Research Letters*, 86(2A), 344–354. <https://doi.org/10.1785/0220140249>
- Wetzler, N., Lay, T., Brodsky, E. E., & Kanamori, H. (2018). Systematic deficiency of aftershocks in areas of high coseismic slip for large subduction zone earthquakes. *Science Advances*, 4(2). <https://doi.org/10.1126/sciadv.aao3225>
- Williams, C. A., & McCaffrey, R. (2001). Stress rates in the central Cascadia subduction zone inferred from an elastic plate model. *Geophysical Research Letters*, 28(10), 2125–2128. <https://doi.org/10.1029/2000GL012623>
- Williams, C. A., & Wallace, L. M. (2015). Effects of material property variations on slip estimates for subduction interface slow-slip events. *Geophysical Research Letters*, 42(4), 1113–1121. <https://doi.org/10.1002/2014GL062505>
- Williams, C. A., & Wallace, L. M. (2018). The impact of realistic elastic properties on inversions of shallow subduction interface slow slip events using seafloor geodetic data. *Geophysical Research Letters*, 45(15), 7462–7470. <https://doi.org/10.1029/2018GL078042>
- Xu, X., Tong, X., Sandwell, D. T., Milliner, C. W., Dolan, J. F., Hollingsworth, J., et al. (2016). Refining the shallow slip deficit. *Geophysical Journal International*, 204(3), 1867–1886. <https://doi.org/10.1093/gji/ggv563>
- Zhu, L., & Kanamori, H. (2000). Moho depth variation in Southern California from teleseismic receiver functions. *Journal of Geophysical Research*, 105(B2), 2969–2980. <https://doi.org/10.1029/1999jb900322>
- Zhu, S., & Zhang, P. (2013). FEM simulation of interseismic and coseismic deformation associated with the 2008 Wenchuan Earthquake. *Tectonophysics*, 584, 64–80. <https://doi.org/10.1016/j.tecto.2012.06.024>